Inorganica Chimica Acta 603 (2026) 123402

Contents lists available at ScienceDirect

Inorganica Chimica Acta

journal homepage: www.elsevier.com/locate/ica

Imidazo-phenanthroline Re(I) complexes with systematic extension in aromaticity as singlet oxygen photosensitizers and CO_2-responsive electrochemical behavior

Patricia M. Toro-Sánchez [a,*], David Villaman [b], Claudio Barrientos [c], Franco Palominos [d], Danilo H. Jara-Quinteros [e,*], Nancy Pizarro [d,*]

[a] Instituto de Ciencias Aplicadas (ICA), Facultad de Ingeniería, Universidad Autónoma de Chile, 5 Poniente 1670, 3467987 Talca, Chile
[b] Laboratorio de Química Inorgánica y Organometálica, Facultad de Cs. Química, Universidad de Concepción, Chile
[c] Centro de Investigación de Estudios Avanzados del Maule (CIEAM), Vicerrectoría de Investigación y Postgrado, Universidad Católica del Maule, Av. San Miguel 3605, Talca 3480112, Chile
[d] Universidad Andrés Bello, Facultad de Ciencias Exactas, Departamento de Ciencias Químicas, Viña del Mar, Chile
[e] Facultad de Ingeniería y Ciencias, Universidad Adolfo Ibáñez, Av. Padre Hurtado 750, Viña del Mar, Chile

ARTICLE INFO

Dataset link: 2541193 (Original data)

Keywords:
Imidazo-phenanthroline
Re(I) complexes
Crystal structure
Singlet oxygen
CO_2 electroreduction

ABSTRACT

We report a homologous series of [Re(CO)$_3$(N—N)Cl] complexes, **Re-nap**, **Re-ant** and **Re-pyr**, based on 1*H*-imidazo[4,5-*f*][1,10]phenanthroline ligands substituted with naphthalen-1-yl (**nap**), anthracen-9-yl (**ant**), and pyren-1-yl (**pyr**) fragments, respectively. The complexes were characterized by ^{1}H NMR, FT-IR, and HRMS, while the solid-state structure of **Re-nap** was established using single-crystal X-ray diffraction. Coordination induces a highly coplanar arrangement of the naphthyl-imidazo-phenanthroline framework, with a dihedral angle of only 2.56(10)° between the phenanthroline and naphthyl fragments, supported by parallel-displaced π-stacking interactions with centroid–centroid distances of 3.800–3.905 Å. Absorption and photoluminescence studies revealed that increasing the aromaticity modulates the interplay between the intraligand (IL), intraligand charge-transfer (ILCT), and metal-to-ligand charge-transfer (MLCT) states. **Re-nap** displayed a distinct MLCT absorption band at 425 nm in CH_2Cl_2 and exhibited the highest MLCT photoluminescence quantum yield of the series, Φ_{PL} = 1.90%, along with a remarkably long ^{3}MLCT lifetime of 9354 ns, compared with 158 ns for **Re-ant** in CH_2Cl_2. All Re(I) complexes efficiently photosensitized singlet oxygen formation upon 405 nm excitation, with Φ_Δ values increasing from 0.708, 0.844, and 0.887 for **Re-nap**, **Re-ant** and **Re-pyr**, respectively. These values exceeded those of the free ligands. Under CO_2, both ligands and complexes displayed enhanced cathodic currents; however, the Re complexes were markedly more responsive, with apparent i_{cat}/i_p ratios of 8.94, 8.80, and 12.0 for **Re-nap**, **Re-ant**, and **Re-pyr**, respectively. These results demonstrate that systematic aromatic extension, particularly through pyrene incorporation, is an effective ligand design strategy for enhancing singlet oxygen photosensitization and CO_2 reduction activity in Re(I) imidazo-phenanthroline complexes.

1. Introduction

1*H*-imidazo[4,5-*f*][1,10]phenanthroline (imidazo-phenanthroline) derivatives have been investigated for their potential applications. Among them, imidazo-phenanthroline (imidazo-phen) ligands have been used for luminescence-based sensing, organic light-emitting devices (OLEDs), molecular switches, and biological applications, including DNA binding and anticancer properties [1–9], and more recently for developing sustainable energy solutions using a hybrid photovoltaic-thermal (PVT) system capable of simultaneously producing electricity and heat [10–12].

The versatility of imidazo-phen derivatives arises from their distinctive structural features. These include *i)* a rigid and planar structure that ensures high thermal stability; *ii)* a π-conjugated system that promotes efficient charge transport and high fluorescence efficiency; *iii)* the coplanarity of the imidazo-phen unit, which facilitates DNA intercalation through π-π interactions, resulting in compounds that exhibit antitumor activity; *iv)* physicochemical properties that can be

* Corresponding authors.
E-mail addresses: patricia.toro@uautonoma.cl (P.M. Toro-Sánchez), danilo.jara.q@uai.cl (D.H. Jara-Quinteros), npizarro@unab.cl (N. Pizarro).

https://doi.org/10.1016/j.ica.2026.123402
Received 4 June 2026; Received in revised form 28 July 2026; Accepted 29 July 2026
Available online 29 July 2026
0020-1693/© 2026 Elsevier B.V. All rights are reserved, including those for text and data mining, AI training, and similar technologies.

easily modified by structural changes (e.g., the imidazole ring of the imidazo-phen moiety can be readily and selectively functionalized at the H1- and C2-positions by introducing different substituents to modulate its optical and electronic characteristics, Fig. S1); and *v)* the nitrogen atoms of the phenanthroline fragment can coordinate with transition metals, resulting in complexes that exhibit strong absorption in the visible region of the solar spectrum, high photoluminescence quantum yields, and long excited-state lifetimes [13–16]. Such flexibility in ligand design allows imidazo-phenanthroline derivatives incorporating metal ions to represent a promising class of materials for visible-light-driven applications across fields, such as photoredox catalysis [17–20], solar energy conversion [21], and therapeutic use [22–27].

In relation to the latter, rhenium(I) tricarbonyl complexes, particularly those with polypyridyl ligands, display remarkable photophysical properties, high biocompatibility, and notable thermal stability [28–30] that can be exploited in various medical applications [31] such as noncovalent luminescent probes [32,33] in biomedical imaging [34,35], and anticancer treatments [36]. Moreover, these complexes are excellent photosensitizers (PS) for generating singlet oxygen ($^1O_2$) [37–42], making them promising candidates for photodynamic therapy (PDT) in oncology [43–45].

Compounds of the general formula [Re(CO)$_3$(N^N)X] [where N^N = 1,10-phenanthroline, 2,2′-bipyridine (bpy), dipyrrinate, 1,2,4-triazolylpyridine, or terpyridine (tpy); and X = halide, pyridine, 2-pyrazine, 2-naphthalene, 9-anthracene, 1-pyrene, 2-anthraquinone, or PPh$_3$] have exhibited long triplet- excited-state lifetimes and high quantum yields of singlet oxygen formation (Φ_Δ), approaching unity [19,29,39,42,46–48]. In most cases, Re(I) complexes can transfer energy to molecular oxygen via the metal-to-ligand charge-transfer triplet excited state (^{3}MLCT). However, ligand-to-ligand charge-transfer (^{3}LLCT), ligand-centered (^{3}LC) triplet-excited electronic configurations, or a combination of these manifolds have also been reported [42,49,50].

A drawback of rhenium(I) complexes that act as PS, mainly [Re(CO)$_3$(N^N)L] derivatives with low-energy π* orbitals, is their lack of high extinction coefficients in the visible region. In this regard, modulating the photosensitizer's electronic properties is crucial for enhancing the quantum yield of $^1O_2$ generation. One possible solution is to design bichromophoric compounds that incorporate naphthalene, pyrene, oligothiophene, or other organic dyes into their structures. The extension of aromaticity can reduce the MLCT energy by stabilizing the π* orbitals, decreasing the HOMO-LUMO gap, and red-shifting the absorption of the complexes [48,51–54]. Additionally, the stabilized LUMO orbitals prolong the lifetimes of the excited states. This enhancement can improve the energy transfer from the ^{3}MLCT excited state to the triplet ground state of oxygen. Consequently, higher singlet oxygen quantum yields are observed, which are essential for PDT applications. Recent studies have reported six Re(I) tricarbonyl complexes containing imidazo-[4,5-*f*][1,10]-phenanthroline ligands [26]. Incorporating this organic moiety enhanced the ^{3}π-π* character of the low-lying triplet excited state, thereby facilitating more efficient photodynamic therapy (PDT). Of the six synthesized molecules, the complex derived from 4-(1-benzyl-1*H*-tetrazol-5-yl)benzaldehyde exhibited exceptional potency and selectivity under yellow light irradiation. The authors attributed this performance to strong absorption in the visible range, an elevated $^1O_2$ quantum yield, and an increased turnover number (TON) for NADH photo-oxidation [26].

Beyond their favorable excited-state properties, rhenium(I) tricarbonyl complexes containing a bidentate diimine ligand feature a catalytically active metal center and a redox-active ligand capable of accumulating multiple electrons for transfer to CO_2 [55–57]. Additionally, the presence of a monodentate axial ligand in the first coordination sphere, which may serve as a leaving group, further enhances the catalytic activity [33]. Since the first report of CO_2 reduction mediated by rhenium complexes, specifically of the type [Re(CO)$_3$(bpy)Cl], published by Lehn et al. in 1983 [58], these compounds have attracted considerable attention because of their remarkable selectivity for CO_2 reduction over proton reduction.

Accordingly, various rhenium-based molecular catalysts incorporating ligands such as bpy, phen, tpy, pyrazolylamidino, dipyridophenazine (dppz), and pyridine-oxazoline have been investigated to enhance the selectivity and efficiency of CO_2 reduction [55,57,59–70].

Building on these advances, ligand design has become a key strategy for modulating the electrocatalytic performance of rhenium(I) complexes. In particular, increasing the π-conjugation of the diimine ligands influences both the electronic structure and the interaction with CO_2. One approach involves incorporating extended aromatic fragments, such as pyrene, into the ligand's scaffold. This modification has been shown to promote CO_2 adsorption and facilitate electron transfer between the complex and CO_2 [71,72], while the associated electronic and steric effects strongly impact the catalytic behavior [73].

Although rhenium diimine complexes (derived from bpy or phen) have been widely studied as singlet-oxygen photosensitizers and CO_2 reduction electrocatalysts, systematic investigations specifically focused on the 1*H*-imidazo[4,5-*f*][1,10]phenanthroline scaffold that simultaneously evaluates the effects of aromatic extension on both photophysical and catalytic properties are limited.

In this study, we aimed to systematically extend the π-system by directly fusing additional chromophore fragments, such as naphthalene, anthracene, and pyrene, to the imidazole ring of phenanthroline to obtain fully conjugated, rigid ligands (Scheme 1). To assess the impact of the three chromophores on the complexes, the ground- and excited-state properties of **Re-nap**, **Re-ant**, and **Re-pyr** compounds were examined and compared. These processes were achieved using steady-state and time-resolved spectroscopic techniques. We also evaluated the effectiveness of rhenium complexes as photosensitizers for generating singlet oxygen ($^1O_2$). Finally, we investigated the preliminary electrocatalytic behavior of all Re(I) compounds toward CO_2 reduction in an aprotic medium.

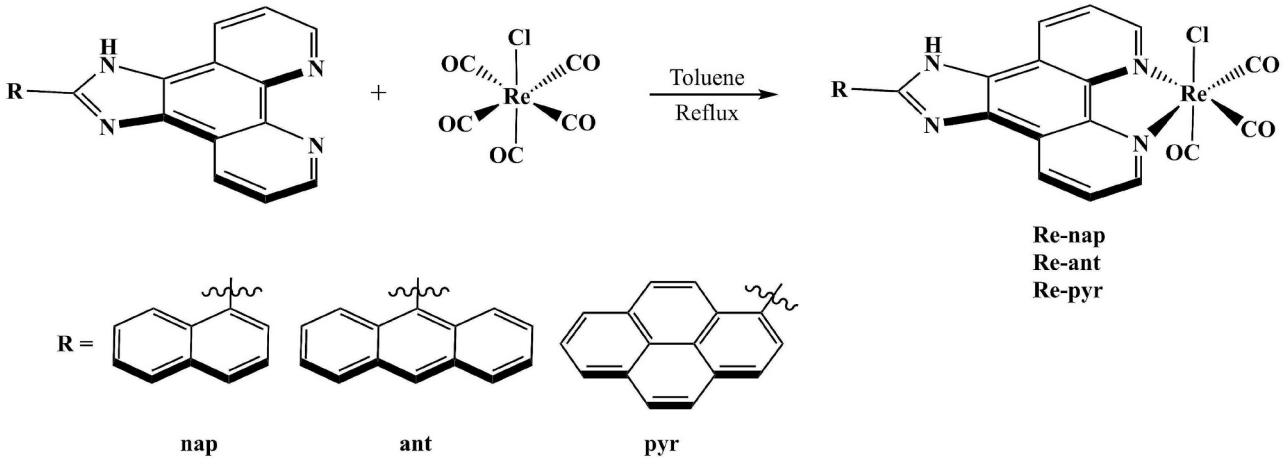
2. Experimental

2.1. General considerations

Re(CO)$_5$Cl (98%) was purchased from Aldrich or AK Scientific, Inc. Dry toluene and spectroscopic-grade dichloromethane (CH_2Cl_2), methanol (MeOH), ethanol (EtOH), and dimethylformamide (DMF) were purchased from Merck. All reagents and solvents were used as received. The 2-(1-naphthalenyl)-1*H*-imidazo[4,5-*f*][1,10]phenanthroline (**nap**), 2-(9-anthracenyl)-1*H*-imidazo[4,5-*f*][1,10]phenanthroline (**ant**), and 2-(1-pyrenyl)-1*H*-imidazo[4,5-*f*][1,10]phenanthroline (**pyr**) ligands were prepared as described in the literature with minor modifications [74,75]. The Electronic Supporting Information (ESI) *experimental section* provides details of the procedures and spectroscopic data for the ligands. High-resolution mass spectrometry (HRMS) spectra were recorded at the *Laboratorio de Servicio de Espectrometría de Masas (Pontificia Universidad Católica de Chile)* using a Bruker compact QTOF MS with direct sample injection. Samples for IR spectroscopy were prepared as KBr pellets and analyzed using a Shimadzu model IR Prestige-21 spectrophotometer in the range of 4000–500 cm^{-1}. ^{1}H NMR spectra were acquired at room temperature on a Bruker Avance 400 spectrometer or a Bruker Avance III HDTM 500 using DMSO-d_6 (99.9%) as the solvent. Chemical shifts (δ), referenced to the deuterated residual solvent peaks, are given in ppm, and the coupling constants (*J*) are reported in Hertz (Hz). The abbreviations for signal multiplicities are as follows: s (singlet), d (doublet), br (broad), ps-d (pseudo-doublet), double-doublet (dd), triplet (t), and m (multiplet).

2.2. Synthesis of complexes. General procedure

Re(CO)$_5$Cl (1.0 mmol) was reacted with an equimolar amount of the corresponding ligand (**nap**, **ant**, or **pyr**) (1.0 mmol) in dry toluene (20 mL) (see Scheme 1). The mixture was refluxed under an argon



Scheme 1. Synthetic route for obtaining rhenium(I) complexes (**Re-nap**, **Re-ant**, and **Re-pyr**).

atmosphere for 5 h. The yellow precipitate was filtered and washed with a minimal amount of toluene (≈ 5.0 mL). The resulting compounds were then dried under vacuum to yield yellow solids.

[$Re(CO)_3$(nap)Cl] (**Re-nap**): [$Re(CO)_5Cl$] (200 mg, 0.55 mmol) and **nap** ligand (191 mg, 0.55 mmol) provided the product as a yellow solid (254 mg, 0.39 mmol, 71%). HRMS (*m/z*): 651.0229 and calc. for {[M] - H}$^+$ $C_{26}H_{14}ClN_4O_3^{187}Re$: 651.0231. FT-IR (KBr, cm^{-1}): 3444 ν(NH), 2025 $\nu(CO)_{Re}$, and 1915 $\nu(CO)_{Re}$. ^{1}H NMR (DMSO-d_6): δ 14.5 (br, 1H, H^7), 9.40 (d, J = 4.9 Hz, 2H, H^1, H^4), 9.34 (d, J = 8.3 Hz, 2H, H^3, H^6), 9.09 (d, J = 8.1 Hz, 1H, $H_{naphthyl}$), 8.20–8.17 (m, 4H, H^2, H^5, $H_{naphthyl}$), 8.11 (d, J = 7.8 Hz, 1H, $H_{naphthyl}$), 7.78 (t, J = 7.7 Hz, 1H, $H_{naphthyl}$), 7.73–7.65 (m, 2H, $H_{naphthyl}$). Single crystals of **Re-nap** suitable for X-ray diffraction were obtained by slow solvent evaporation from a dichloromethane/DMF mixture.

[$Re(CO)_3$(ant)Cl] (**Re-ant**): [$Re(CO)_5Cl$] (200 mg, 0.55 mmol) and **ant** ligand (218 mg, 0.55 mmol) provided the product as a yellow solid (302 mg, 0.43 mmol, 79%). HRMS (*m/z*): 701.0385 and calc. for {[M] - H}$^+$ $C_{30}H_{16}ClN_4O_3^{187}Re$: 701.0388. FT-IR (KBr, cm^{-1}): 3393 ν(NH), 2022 $\nu(CO)_{Re}$, 1896 $\nu(CO)_{Re}$. ^{1}H NMR (DMSO-d_6): δ 9.42 (d, J = 4.8 Hz, 2H, H^1, H^4), 9.24 (ps-d, J = 8.0 Hz, 2H, H^3, H^6), 8.94 (s, 1H, $H_{anthracenyl}$), 8.27 (d, J = 8.5 Hz, 2H, $H_{anthracenyl}$), 8.18 (dd, J = 8.3, 5.2 Hz, 2H, H^2, H^5), 7.82 (d, J = 8.8 Hz, 2H, $H_{anthracenyl}$), 7.62 (t, J = 7.5 Hz, 2H, $H_{anthracenyl}$), 7.53 (t, J = 7.9 Hz, 2H, $H_{anthracenyl}$).

[$Re(CO)_3$(pyr)Cl] (**Re-pyr**): [$Re(CO)_5Cl$] (200 mg, 0.55 mmol) and **pyr** ligand (232 mg, 0.55 mmol) provided the product as a yellow solid (350 mg, 0.48 mmol, 87%). HRMS (*m/z*): 725.0379 and calc. for {[M] - H}$^+$ $C_{32}H_{18}ClN_4O_3^{187}Re$: 725.0388. FT-IR (KBr, cm^{-1}): 3422 ν(NH), 2026 $\nu(CO)_{Re}$, and 1918 $\nu(CO)_{Re}$. ^{1}H NMR (DMSO-d_6): δ 14.6 (br, 1H, H^7), 9.51 (d, J = 9.4 Hz, 1H, $H_{pyrenyl}$), 9.41 (d, J = 4.3 Hz, 2H, H^1, H^4), 9.36 (d, J = 8.1 Hz, 2H, H^3, H^6) 8.69 (d, J = 8.1 Hz, 1H, $H_{pyrenyl}$), 8.54 (d, J = 8.1 Hz, 1H, $H_{pyrenyl}$), 8.39 (d, J = 7.9 Hz, 3H, $H_{pyrenyl}$), 8.32–8.27 (m, 2H, $H_{pyrenyl}$), 8.20–8.14 (m, 3H, H^2, H^5, $H_{pyrenyl}$).

2.3. Crystal structure determination

Crystals suitable for **Re-nap** were selected for single-crystal X-ray diffraction (SC-XRD) analysis. Data collection was performed at 296 K using a Bruker D8 Venture diffractometer equipped with a CMOS Photon III 14 detector and an IμS 3.0 microfocus source with Mo-Kα radiation (λ = 0.71073 Å). Crystallographic frames were collected and integrated using APEX4 software [76], with absorption corrections applied using SADABS [77]. The molecular structure was solved using the Intrinsic Phasing method implemented in ShelXT [78] and refined through full-matrix least-squares based on F^2 using ShelXL [79], all within the Olex2 interface [80]. Hydrogen atoms were placed in calculated positions and refined with isotropic displacement parameters, whereas all other atoms were refined with anisotropic thermal parameters. A solvent mask was applied, revealing the presence of 784 electrons within a void volume of 2484 Å^3 per unit cell. This is consistent with the inclusion of a toluene solvent molecule (C_7H_8 per formula unit) in the crystal structure. ORTEP plots were generated using Olex2 software [80].

2.4. Photophysical measurements

Ultraviolet–visible (UV–Vis) absorption spectra were recorded on an Agilent Cary 8454 Diode-Array Spectrophotometer over the range 250–800 nm in aerated CH_2Cl_2 and DMF solutions at room temperature (RT). Dispersions were passed once by gravity through a tightly packed plug of cotton wool placed in a micropipette tip. The cotton wool was pre-rinsed with the solvent before use. No vacuum was applied. This coarse-filtration step was intended solely to remove undissolved particles, and the resulting filtrate was used immediately or diluted for characterization. Photoluminescence (PL) spectra were measured in CH_2Cl_2 and DMF solutions saturated with argon gas using a Horiba Jobin-Yvon FluoroMax-4CP spectrofluorometer at RT. The photoluminescence quantum yields (Φ_{PL}) were evaluated using the procedures described in the literature, with $[Ru(bpy)_3](PF_6)_2$ as the actinometer [81]. Photoluminescence lifetime measurements were performed using a PicoQuant FluoTime 300 fluorescence lifetime spectrometer with a time-correlated single-photon counting technique. Picosecond lasers of 375 and 405 nm were employed as pulsed light sources (FWHM: ~ 54 ps; average power: 31 pJ). For the detection of emission at 1270 nm, an NIR detector PMT H10330A (Hamamatsu) was employed. The $^1O_2$ quantum yield (Φ_Δ) was determined in CH_2Cl_2 by comparing the intensity at zero time of the 1270 nm signals with those of optically matched solutions of perinaphthenone (PNF) as a reference (Φ_Δ = 0.98 in CH_2Cl_2) [82,83]. Phosphorescence emission spectra of singlet oxygen generated by PNF and the studied compounds upon excitation at 405 nm were recorded using the steady-state measurement mode of the FluoTime300 spectrometer.

2.5. Electrochemical studies

Cyclic voltammograms were recorded at room temperature using a CHI 650E potentiostat in a three-electrode cell. A platinum wire (CHI115) was used as the counter electrode, Ag/AgCl (CHI111) as the reference electrode in a Luggin capillary, and a glassy carbon (CHI104) as the working electrode. Each complex was dissolved in DMF containing 0.1 M tetra-*n*-butylammonium hexafluorophosphate ($TBAPF_6$) as the supporting electrolyte, yielding a final concentration of 1 mM for the measurements. All experiments were conducted in a cell previously degassed with N_2. For the electrocatalytic CO_2 studies, the cell was

saturated with CO_2. The measurements were performed over the potential range from −2.40 to 0.00 V, and scan rates ranging from ν = 0.100 to 1.00 Vs^{-1} were examined.

3. Results and discussion

3.1. Synthesis and characterization of the complexes

1*H*-imidazo[4,5-*f*][1,10]phenanthroline ligands bearing naphthalene (**nap**), anthracene (**ant**), or pyrene (**pyr**) were selected to investigate the influence of systematic aromatic extension on the photophysical and electrochemical properties of the three complexes. The complex **Re-ant** was synthesized via an equimolar reaction between $Re(CO)_5Cl$ and the 2-(9-anthracenyl)-1*H*-imidazo[4,5-*f*][1,10]phenanthroline ligand (**ant**) in dry toluene. The reaction mixture was stirred under reflux for 5 h in an argon atmosphere, affording the **Re-ant** complex in a 79% yield. The **Re-nap** and **Re-pyr** complexes have been previously reported [19,54]. All the complexes were characterized by HRMS (Figs. S2 – S4), FT-IR (Figs. S5 - S7), and ^{1}H NMR spectra (Figs. S8 – S10). In addition, assignments ^{1}H were confirmed by 2D ^{1}H—^{1}H COSY NMR experiments in DMSO-d_6 (Figs. S11 - S13). The syntheses of the bidentate ligand precursors and rhenium(I) complexes are summarized in Schemes S1 and 1, respectively. Experimental details are provided in the ESI.

The structure of the **Re-nap** complex was determined by single-crystal X-ray diffraction (SC-XRD) analysis at 296 K. The compounds were further characterized by steady-state and time-resolved photoluminescence spectroscopy in solution at room temperature, as detailed below.

3.2. Single-crystal X-ray diffraction

The synthesis and spectroscopic characterization (IR and NMR) of the naphthyl derivative (**Re-nap**) have been reported previously [54]. Nevertheless, its solid-state structure has not been elucidated, despite the recognized importance of intermolecular contacts in chromophoric systems. To address this gap, suitable single crystals of this compound for X-ray diffraction were obtained by slowly diffusing dichloromethane into a DMF solution. The structure of the complex and its labeling are shown in Fig. 1. The crystallographic details are summarized in Table S1, and the selected bond lengths and angles are listed in Table S2.

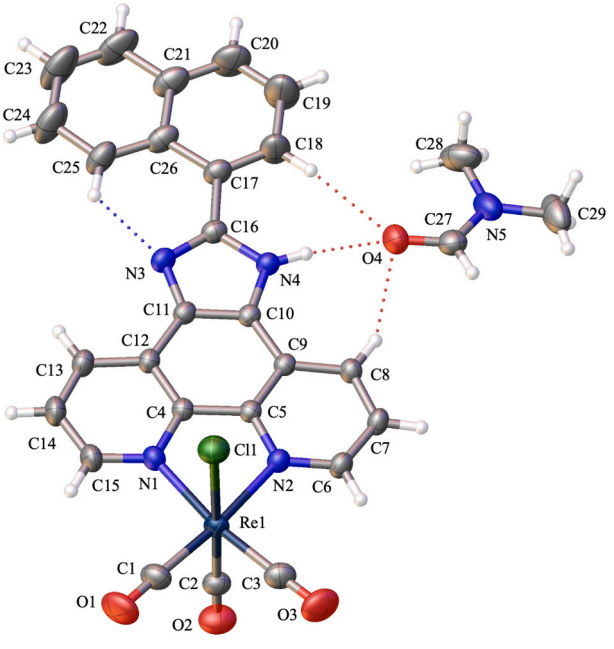


Fig. 1. ORTEP plot of the **Re-nap** compound. Thermal ellipsoids are shown at 30% of probability.

The **Re-nap** complex crystallized in the centrosymmetric tetragonal $I4_1/a$ space group (Z = 16; Z' = 1) and adopted a distorted octahedral geometry (Fig. 1), with a total deviation across the twelve ideal 90° angles of 56.7(4)° $\left(\Sigma = \sum_{i=1}^{12} |\phi_i - 90^\circ|\right)$. The three carbonyl ligands exhibited a *fac*-type geometry, which is common in Re(I)-derived tricarbonyl complexes with chloride counterions in the apical position [19,84–86]. The Re(I)–C distances were within the expected range for this type of complex, with an average of 1.906 Å. The remaining two coordination sites were occupied by a chelating derivative of imidazo[1,10]phenanthroline with average Re(I)–N bond distances of 2.174 Å, as expected for these analogous systems [43,87,88].

To elucidate the structural features of the **Re-nap** complex, especially the conformation of the coordinated ligand, a comparison with previously reported crystallographic data for the free **nap** ligand is highly informative [75]. In the solid state, the uncoordinated ligand displayed a significant dihedral angle exceeding 40° between the naphthyl and phenanthroline fragments, indicative of a non-planar molecular structure [75]. However, upon coordination to a metal center, the naphthyl fragment undergoes rotation, facilitating intramolecular interactions with counterions or, in this case, with the molecular solvent (DMF), resulting in a high degree of coplanarity throughout the molecule.

The dihedral angle between the plane defined by atoms (C4–C5–C9–C10–C11–C12) of the phenyl substituent attached to the imidazole ring of the phenanthroline core and the plane formed by atoms (C17–C18–C19–C20–C21–C26) of the naphthyl fragment was 2.56(10)°, suggesting a high coplanarity across the entire system. This planarity enables efficient electronic communication within the molecule. It is attributed to parallel displacement π–stacking interactions in the supramolecular structure, specifically between *Cg*1···*Cg*5^{ii}, *Cg*2···*Cg*4^{ii}, and *Cg*3···*Cg*4^{ii}, with centroid–centroid distances of 3.878, 3.905, and 3.800 Å, respectively (Table 1, Fig. S14).

Analysis of the crystal packing revealed weak interactions, specifically N–H···O, C–H···O, and C–H···N contacts (Table 2). The strongest intramolecular interactions were N4–H4···O4 (graph set *motif* D_1^1 (2)), and C25–H25···N3 (graph set *motif* S_1^1 (6)), with donor-acceptor (D-A) distances of 2.809 Å and 2.889 Å, respectively. The presence and spatial arrangement of these interactions are also likely to help prevent twisting of the naphthyl fragment, thereby enhancing electronic communication.

The connectivity and stability of the packing are determined by the intermolecular contacts C6–H6···O1^1, C7–H7···O1^1, C24–H24···O2^2, and C25–H25···O2^2, with both pairs corresponding to bifurcated hydrogen bonds. The first set of contacts generates a two-dimensional layer in the *ab* plane (Fig. S15), characterized by R_4^4 (24) and R_4^4(28) ring-type graph-set *motif*. The second set, involving atom O2^2, is connected to a second layer within the same plane.

3.3. Photophysical characterization

3.3.1. Electronic absorption and photoluminescence spectroscopy

The absorption spectra of **nap**, **ant**, **pyr**, **Re-nap**, **Re-ant**, and **Re-pyr** compounds measured at RT in CH_2Cl_2 and DMF are shown in Figs. 2–4.

Table 1
Intermolecular π–2π stacking interactions of the Re(I) complex.

Centroid	*Cg*–*Cg* distance/Å	Shift distance/Å	Angle/°
*Cg*1···*Cg*5^{ii}	3.878	1.823	3.017
*Cg*2···*Cg*4^{ii}	3.905	1.775	4.090
*Cg*3···*Cg*4^{ii}	3.800	1.525	3.462

^{ii}1/4 + y,5/4-x,1/4 + z
*Cg*1 = C4/C12/C11/C10/C9/C5; *Cg*2 = C17/C26/C21/C20/C19/C18; *Cg*3 = C25/C26/C21/C22/C23/C24;
*Cg*4^{ii} = N1/C15/C14/C13/C12/C4; *Cg*5^{ii} = N2/C67/C7/C8/C9/C5

Table 2
Intra- and intermolecular hydrogen bonds of the **Re-nap** complex.

D–H···A	d(D—H)/Å	d(H-A)/Å	d(D-A)/Å	D-H-A/°
N4–H4···O4	0.86	1.96	2.809(3)	171.9
C25–H25···N3	0.93	2.21	2.889(3)	129.0
C6–H6···O1[1]	0.93	2.59	3.230(3)	126.7
C7–H7···O1[1]	0.93	2.65	3.251(3)	122.7
C24–H24···O2[2]	0.93	2.81	3.401(5)	122.4
C25–H25···O2[2]	0.93	2.77	3.378(4)	124.3

[1]1/4 + y,3/4-x,3/4-z; [2]1/4 + y,5/4-x,1/4 + z

The ligands and complexes exhibited limited solubility in CH_2Cl_2; therefore, the solutions were filtered to prevent PL emission arising from dispersion [89]. To address this limitation, DMF was employed as the solvent because it provides improved solubility for the samples. In this solvent, UV–Vis absorption spectra were recorded across a concentration range of 10^{-5} to 10^{-6} M to determine molar extinction coefficients (ε) and verify the absence of concentration-dependent spectral changes. The corresponding data and plots are available in ESI (Figs. S16 and S17).

For all the ligands in both solvents, the absorption bands between 230 and 450 nm can be attributed to intraligand (IL) π → π* transitions centered on the imidazo-phen ($\pi_{imidazo\text{-}phen} \rightarrow \pi^*_{imidazo\text{-}phen}$), or polyaromatic moieties ($\pi_{nap/ant/pyr} \rightarrow \pi^*_{nap/ant/pyr}$), and intraligand charge transfer (ILCT) ($\pi_{nap/ant/pyr} \rightarrow \pi^*_{imidazo\text{-}phen}$) (Figs. 2–4) [75,90]. For **Re-ant** and **Re-pyr,** a metal-to-ligand charge transfer (MLCT) ($d\pi_{Re} \rightarrow \pi^*_{imidazo\text{-}phen}$) transition was observed in the 350–550 nm region, overlapping with the IL and ILCT transitions of the corresponding ligands (Figs. 3 and 4). In contrast, for **Re-nap**, the MLCT ($d\pi_{Re} \rightarrow \pi^*_{imidazo\text{-}phen}$) band in CH_2Cl_2 exhibited a maximum wavelength of 425 nm, whereas in DMF, it appeares as a shoulder accompanied by a broad, low-intensity tail (Fig. 2). The maximum absorption wavelengths (λ_{max}) of the ligands and complexes in CH_2Cl_2 and DMF are summarized in Table 3.

Steady-state photoluminescence (PL) spectra at room temperature were recorded for all the ligands and complexes in CH_2Cl_2 and DMF purged with argon (Figs. 2–4). The corresponding PL parameters are listed in Table 3. For **nap** and **pyr** ligands, two excitation-dependent PL spectra were observed in both solvents, with λ_{max} = 400–450 nm (blue-side band) and λ_{max} = 520–560 nm (red-side band). The first band emerged under irradiation with short-wavelength excitation, whereas the second band became progressively more intense as the excitation wavelength increased and became dominant at longer excitation wavelengths (Fig. S18A,C, and S20A,C). This behavior was more pronounced for **nap**, while **pyr** exhibited a clean blue-side band under high-energy excitation. The PL emission at high energy can be attributed to fluorescence from the ^{1}IL ($^1(\pi \rightarrow \pi^*_{(imidazo\text{-}phen)})$) and ^{1}IL ($^1(\pi \rightarrow \pi^*_{(pyr)})$) excited states for **nap** and **pyr**, respectively. The PL spectrum of **pyr** in CH_2Cl_2 displayed vibronically structured emission (Fig. 4A), a characteristic signature of fluorescence in polycyclic aromatic molecules. In contrast, the **ant** ligand exhibited a single excitation-independent emission band at 498 nm (CH_2Cl_2) and 483 nm (DMF) (Fig. S19A,C). This single band for **ant** and the red-side emission bands observed in **nap** and **pyr** can be assigned to fluorescence from the ^{1}ILCT ($\pi_{nap} \rightarrow \pi^*_{imidazo\text{-}phen}$), ^{1}IL ($^1(\pi \rightarrow \pi^*_{ant})$)/^{1}ILCT ($\pi_{ant} \rightarrow \pi^*_{imidazo\text{-}phen}$), and ^{1}ILCT ($\pi_{pyr} \rightarrow \pi^*_{imidazo\text{-}phen}$) excited states for **nap**, **ant** and **pyr**, respectively, according to theoretical calculations reported in a previous study [91].

The dual excitation-dependent emissions of **nap** and **pyr**, together with the single emission observed for **ant** suggest different efficiencies of

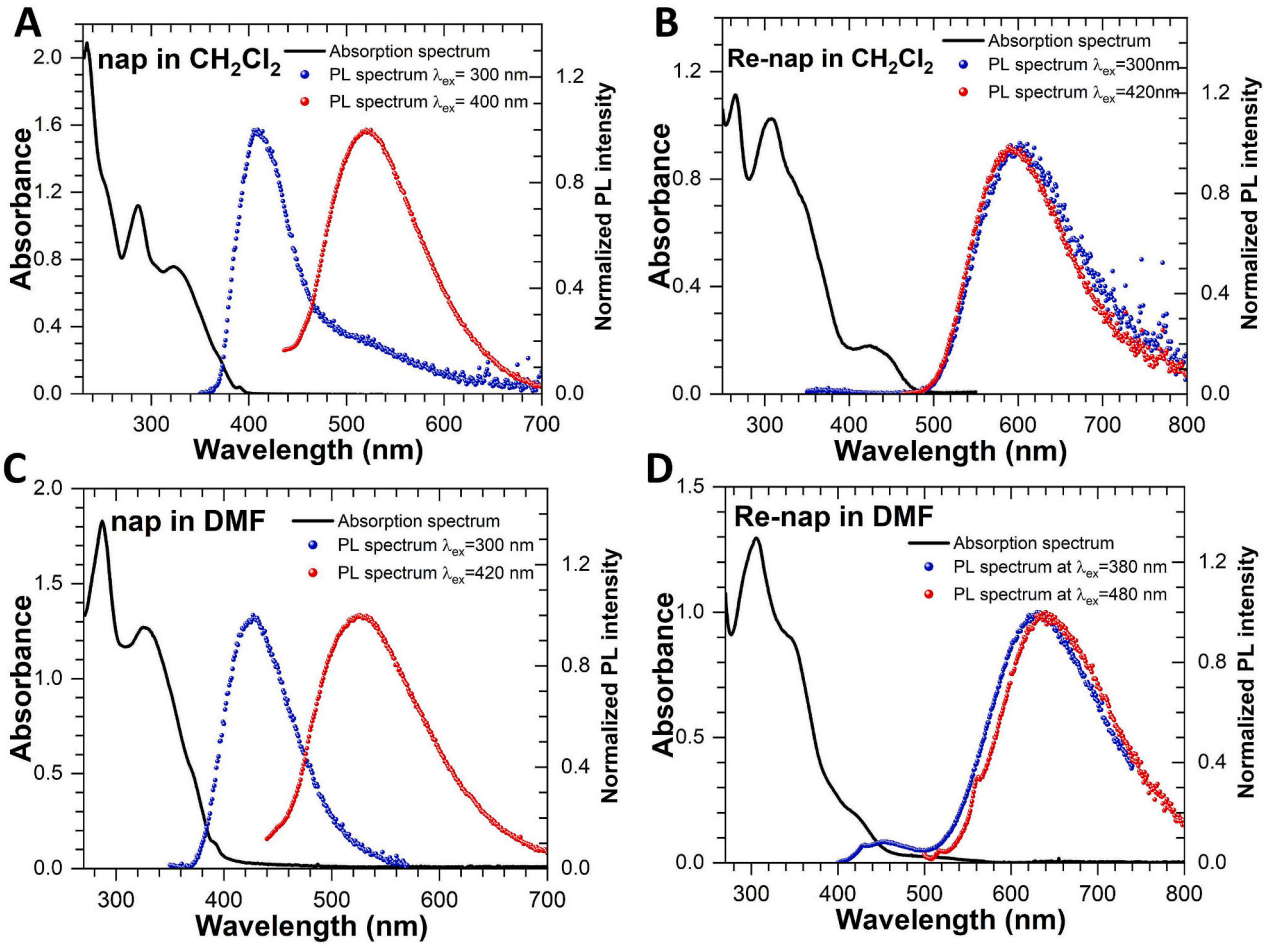


Fig. 2. Absorption and photoluminescence spectra at two excitation wavelengths, **nap** and **Re-nap**, in CH_2Cl_2 (**A** and **B**) and DMF (**C** and **D**) at RT.

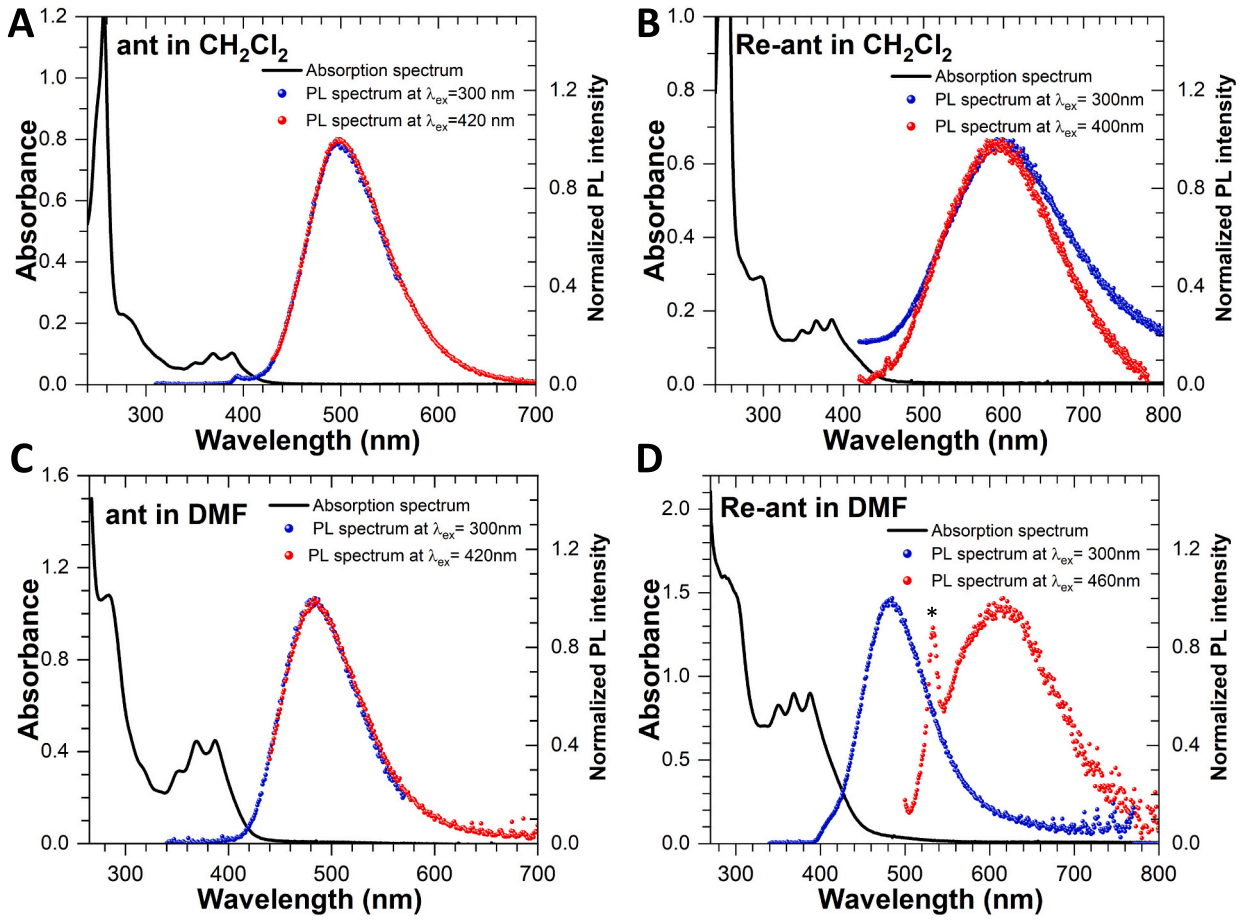


Fig. 3. Absorption and photoluminescence spectra at two excitation wavelengths of **ant** and **Re-ant** in CH_2Cl_2 (**A** and **B**) and DMF (**C** and **D**) at RT. * This signal is attributed to Raman from DMF.

intramolecular electronic energy transfer (Φ_{EET}) from the naphthalene/anthracene/pyrene (donors) to the imidazo-phen (acceptor) fragment. For **ant**, Φ_{EET} should approach unity in both CH_2Cl_2 and DMF, as no blue-side emission band was detected at any excitation wavelength. This assignment is consistent with the results reported by Mondal et al. [92], who estimated the Φ_{EET} of **ant** to be close to one, indicating a rapid and highly efficient intra-EET process, dominated by the Dexter through-space exchange-interaction mechanism. In contrast, the observation of dual emission in **nap** and **pyr** may indicate inefficient EET from the naphthalenyl/pyrenyl moieties to the imidazo-phen fragment, thereby allowing their localized excited states to emit independently.

For **nap** and **pyr**, the excitation spectra recorded at the emission maximum of the red-side band in both CH_2Cl_2 and DMF resembled their absorption spectra (Figs. S21A,C and S23A,C), indicating that the lower-energy emissive state is accessed via the same electronic transitions observed in the ground-state absorption manifold. In contrast, the excitation spectra collected at the blue-side emission maximum were shifted to higher energies (i.e., were blue-shifted) relative to the absorption spectra (Figs. S21A,C and S23A,C), demonstrating that the blue-side emission originates from higher-energy IL transitions that do not efficiently funnel into the red-side emissive state. This spectral mismatch provides additional evidence for distinct excitation pathways underlying the dual-emission behavior of these molecules. For **ant**, the excitation spectrum in both CH_2Cl_2 and DMF mirrored the absorption spectrum regardless of the monitored emission wavelength. This consistency supports the presence of a single emitting state (Fig. S22A,B).

The PL lifetimes of **nap** and **pyr** in both CH_2Cl_2 and DMF were biexponential, with $\tau_1 = 1–2$ ns (blue-side band) and $\tau_2 = 5–16$ ns (red-side band) (Figs. S24 and S26). For **ant,** however, a single-exponential decay with $\tau = 5$ ns was observed in both solvents (Fig. S25). These lifetimes are consistent with fluorescence arising from the IL or ILCT excited states.

The **Re-nap**, **Re-ant**, and **Re-pyr** complexes also exhibited distinct PL properties. In CH_2Cl_2, both **Re-nap** and **Re-ant** displayed a single PL emission band at all excitation wavelengths, centered at approximately 600 nm, and assigned to a ^{3}MLCT excited state (Figs. 2B and 3B). In contrast, **Re-pyr** did not show detectable ^{3}MLCT emission under these conditions; instead, dual-ligand-based emissions were observed (Fig. 4B). In DMF, all complexes exhibited ^{3}MLCT emission upon irradiation at longer wavelengths, whereas IL/ILCT-centered fluorescence was detected under high-energy excitation (Figs. 2D, 3D, and 4D). The coexistence of ligand-centered and charge-transfer emissions has previously been described for Re(I) imidazo-phenanthroline complexes, in which solvent polarity and specific hydrogen-bonding interactions with the imidazole NH group modulate the relative energies and populations of the IL, ILCT, and MLCT excited states [19,93].

The excitation spectra of **Re-nap**, **Re-ant**, and **Re-pyr**, recorded at the maxima of their respective^{3}MLCT emissions in both CH_2Cl_2 and DMF (Figs. S21B,D; S22B,D; and S23D), resembled their absorption profiles, indicating that the electronic transitions decaying to the ^{3}MLCT state correspond to those observed in the absorption spectrum.

PL quantum yields of the ^{3}MLCT emission were determined in deoxygenated CH_2Cl_2 for **Re-nap** and **Re-ant**, for which a single MLCT emission band was observed. **Re-nap** exhibited the higher quantum yield, whereas the lower value for **Re-ant** was attributed to an increased non-radiative decay to populate other excited states. Due to the weak PL intensity of **Re-pyr** in CH_2Cl_2, its PL quantum yield could not be determined. It is possible that the excited-state decay of **Re-ant** and **Re-**

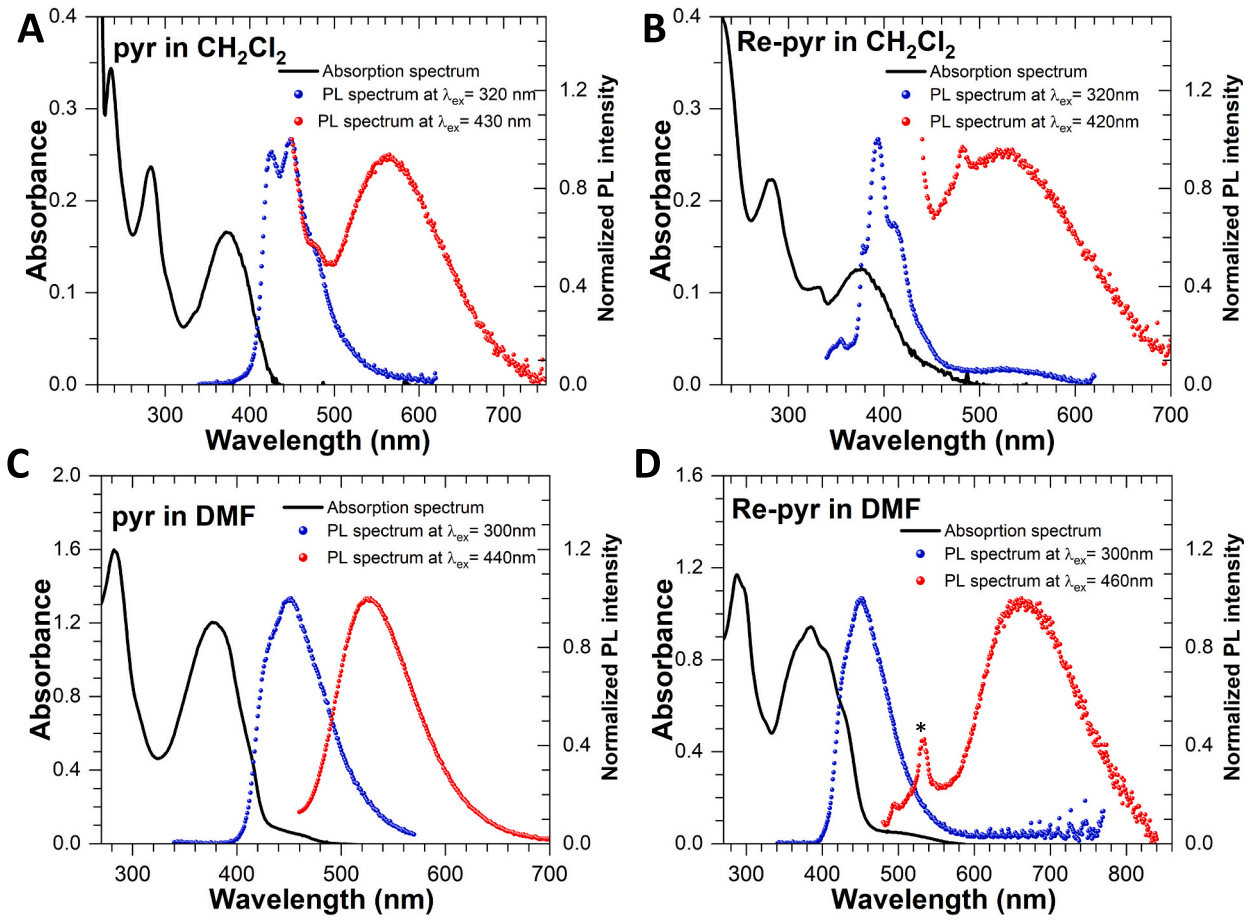


Fig. 4. Absorption and photoluminescence spectra at two excitation wavelengths of **pyr** and **Re-pyr** in CH_2Cl_2 (**A** and **B**) and DMF (**C** and **D**) at RT. * This signal is attributed to Raman from DMF.

Table 3
Photophysical properties of the ligands and respective Re(I) complexes in CH_2Cl_2 and DMF at room temperature.

Compound	λ^a_{abs}, nm [ε, M^{-1} cm^{-1}]		λ^b_{PL} (λ_{ex})^c, nm		Φ^d_{PL}(%)	τ^f_{PL}, ns (f^{int})^g [(λ_{ob}, nm]	
	CH_2Cl_2	DMF	CH_2Cl_2	DMF		CH_2Cl_2	DMF
Nap	234, 258 (sh), 286, 324, 390	287, 327, 392 (sh)	410 (300), 520 (400)	428 (300), 528 (420)	–	0.63 ± 0.01 (18%), 5.87 ± 0.14 (82%) [420]; 10.80 ± 0.04 [520]	0.65 ± 0.01 (51%), 6.61 ± 0.07 (49%) [420]; 4.41 ± 0.19 (11%), 16.40 ± 0.19 (89%) [520]
Ant	256, 280 (sh), 350, 369, 388	283, 319 (sh), 352, 369, 387	498 (300 and 420)	483 (300 and 420)	–	4.98 ± 0.02 [500]	4.63 ± 0.02 [530]
Pyr	235, 283, 374	282, 378, 453 (tail)	426, 448, 478 (sh) (320) 563 (430)	450 (300), 526 (440)	–	1.63 ± 0.01 [420]; 1.74 ± 0.03 (36%), 10.0 ± 0.08 (64%) [560]	1.95 ± 0.01 [480]; 1.98 ± 0.01 (86%), 4.82 ± 0.08 (14%) [530]
Re-nap	265, 306, 345 (sh), 425	305 [29,827], 348 (sh) [19,677], 421 (sh) [4539], 507 (tail) [480]	597 (300 and 420)	450, 630 (380), 640 (480)	1.90 ± 0.07	9354 ± 117 [600]	1004 ± 9 [630]
Re-ant	254, 298, 348, 366, 386	295 (sh) [21,667], 349 [11,402], 368, [12,686], 388, [12,826], 496 (tail) [398]	595 (300 and 400)	483 (300), 615 (460)	1.50 ± 0.29	158 ± 6 (50%), 10.4 ± 0.4 (50%) [600]	4.63 ± 0.02 [480]; 100 ± 3 [620]
Re-pyr	234, 281, 331, 373, 450 (tail)	284 [46,023], 374 [33,904], 405 (sh) [23,137], 510 (tail) [1143]	377 (sh), 392, 414 (sh), 530 (320), 530 (420)	450 (300), 660 (460)	–^{e}	2.53 ± 0.05 (36%), 10.6 ± 0.1 (64%) [530]	1.92 ± 0.01 [450]; –- [660]^h

^{a} Maximum UV–Vis absorption wavelength. ^{b} PL maximum value of the wavelength in nm. ^{c} Excitation wavelength. ^{d} Photoluminescence quantum yield in CH_2Cl_2 from MLCT, with $[Ru(bpy)_3(PF_6)_2]$ as the standard. ^{e} Due to the low intensity, it was not possible to calculate. ^{f} λ_{ex} = 405 nm. ^{g} Fractional intensity of PL lifetime. ^{h} Due to the low intensity, detection was not possible.

pyr evolves to the anthracene or pyrene located triplet excited state, as has been reported for other complexes having these fragments [46,90].

The PL lifetimes recorded at 405 nm and monitored at the ^{3}MLCT emission maximum were τ = 9354 ns for **Re-nap** and τ =158 ns for **Re-**

ant in CH_2Cl_2, and τ =1004 ns and τ =100 ns, respectively, in DMF (Figs. S27 and S28). In addition, the **Re-ant** lifetime in CH_2Cl_2 fitted a biexponential decay, with a short-lived decay of 10 ns, indicating that some IL component is overlapping the ^{3}MLCT emission band (Fig. S25). For **Re-pyr**, the lifetime of the emission from the ^{3}MLCT state could not be detected due to its very low signal intensity when excited at 405 nm. We could not measure at lower excitation energy because of instrumental limitations. However, Choroba et al. reported a very long PL lifetime for **Re-pyr** in DMSO at λ_{ex} = 420 nm [19]. In the present study, the remarkably long ^{3}MLCT lifetime observed for **Re-nap** in CH_2Cl_2 can be rationalized in terms of the electronic and structural characteristics of the **nap** ligand. TD-DFT analyses of the free ligand and crystal structure of **Re-nap** indicate that the naphthyl-substituted imidazo-phen retains a relatively well-defined frontier-orbital distribution and a largely planar geometry, resulting in a more rigid excited-state structure and diminishing the efficiency of non-radiative pathways. In contrast, the anthryl analog exhibits a pronounced distortion of approximately 57° between the anthracene and imidazo-phen fragments [91], leading to reduced π-conjugation and enhanced vibrational flexibility that facilitates non-radiative decay (internal conversion or intersystem crossing) to populate a triplet excited state localized on the anthracene group, which may explain why **Re-ant** displays a much shorter ^{3}MLCT lifetime. This pathway is more efficient for the ^{3}MLCT of **Re-pyr**, in which the emission would be almost completely quenched by the lower-lying triplet excited state of pyrene. For **Re-nap**, the more rigid and electronically isolated ^{3}MLCT state suppresses non-radiative deactivation pathways, resulting in a lifetime nearly two orders of magnitude longer than that of **Re-ant**.

3.3.2. *Singlet oxygen generation studies*

Photosensitized singlet oxygen generation is an important parameter for cancer treatment via PDT [94]. Therefore, the singlet oxygen quantum yields (Φ_Δ) of Re(I) compounds (**Re-nap**, **Re-ant**, and **Re-pyr**) were measured in CH_2Cl_2, and their values are summarized in Table 4. All Re(I) complexes were able to sensitize the generation of singlet oxygen upon excitation at 405 nm. For comparison, Φ_Δ values for free ligands were also determined. Moreover, direct experimental evidence of singlet oxygen generation by the studied compounds upon excitation at 405 nm was obtained by measuring their characteristic phosphorescence emission band with a maximum at 1270 nm (see Fig. S30). As shown in Fig. 5 and in Table 4, the Φ_Δ values of the complexes are notably higher than those for the free ligands, indicating the greater ability of **Re-nap**, **Re-ant**, and **Re-pyr** for $^1O_2$ generation. The increased values of around 2–3 times may arise from a photosensitized contribution from ^{3}MLCT and ^{3}IL/^{3}ILCT excited states. Moreover, the higher values for **Re-ant** and **Re-pyr** approximately correlate with the lower-lying triplet excited-state energies of the anthracenyl and pyrenyl fragments (Table 4), demonstrating that structural modifications can markedly enhance the capacity for singlet oxygen photosensitization. The low Φ_Δ value for **Re-nap** is consistent with its highest emissive capacity and also with the high energy of the naphthyl triplet excited state. (See Table 5.)

In this context, it is important to consider not only modulating the HOMO-LUMO gap or stabilizing the LUMO of the photosensitizer, but also the energies of the excited states of each component or fragment of bichromophoric systems to increase the singlet oxygen generation quantum yield.

Based on our results, the imidazo-phenanthroline scaffold, which offers structural rigidity and aromatic extension, achieves near-unity singlet oxygen yields (0.887 for **Re-pyr**), underscoring its innovation and utility as a multifunctional framework compared to traditional diimine systems.

Table 4
Singlet oxygen quantum yields of free ligands and Re(I) complexes in CH_2Cl_2 solution. Triplet energy (E_T) of aromatic fragments (naphthalene, anthracene, pyrene).

Compound	Φ_Δ [a]	E_T (eV)
Nap	0.250 ± 0.020	2.64[b]
Ant	0.283 ± 0.030	1.82[c]
Pyr	0.260 ± 0.005	2.08[d]
Re-nap	0.708 ± 0.037	
Re-ant	0.844 ± 0.019	
Re-pyr	0.887 ± 0.032	

[a] λ_{ex} = 405 nm. [b] From ref. [95]. [c] From ref. [96]. [d] From ref. [97].

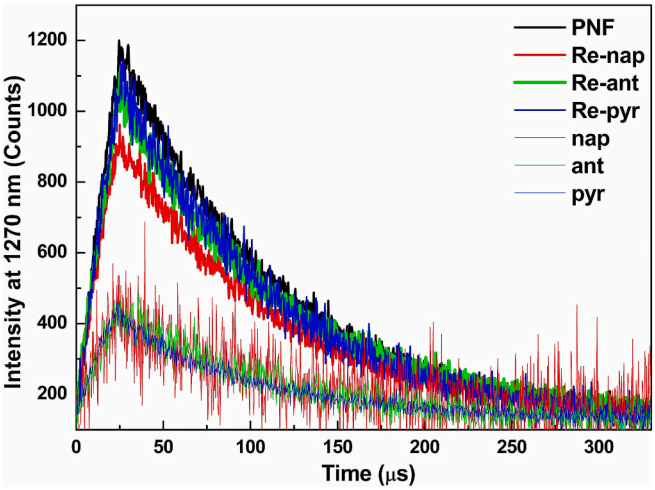


Fig. 5. Singlet oxygen phosphorescent decay generated upon excitation of free ligands and Re(I) complexes in CH_2Cl_2 solutions (λ_{ex} = 405 nm). PNF was used as a reference.

3.4. *Electrochemical properties*

The electrochemical properties of the ligands (**nap**, **ant**, and **pyr**), and their respective Re(I) complexes (**Re-nap**, **Re-ant**, and **Re-pyr**) were investigated using cyclic voltammetry (CV). Cyclic voltammograms were performed in N_2-saturated DMF solutions containing 1 mM of ligand or Re-complex and 0.1 M $TBAPF_6$ as the supporting electrolyte at different scan rates (Figs. S31 and S32).

At a scan rate of 0.1 Vs^{-1}, the voltammograms for all ligands and Re(I) compounds in the cathodic branch are shown in Figs. S33 and 6. Their reduction potentials are summarized in Table 5 and Table S4.

At a scan rate of 0.1 Vs^{-1}, the cyclic voltammograms of the ligands (Fig. S33) showed an intense cathodic peak close to −2.0 V vs Ag/AgCl, which is characteristic of this type of structure, for which the electrochemical processes typically occur around −2.0 V or more negative potentials [98]. This peak was fully irreversible for **nap** (−2.210 V). In contrast, **ant** (−2.052 V) and **pyr** (−2.118 V) exhibited quasi-reversible behavior with peaks observed in the reverse scan, yielding ΔE_p values of 84 mV and 70 mV, respectively. These cathodic waves appeared at relatively negative potentials, consistent with ligand-centered reduction processes followed by chemical or structural relaxation. The low-intensity peaks, observed between −0.7 V and − 1.5 V, were not considered for signal assignment purposes.

Table 5
Summary of electrochemical data for **Re-nap**, **Re-ant**, and **Re-pyr** in DMF solution under N_2 atmosphere. [a]

Compound	E_1 (V)	E_{1r} (V)	E_2 (V)	E_{2r} (V)	ΔE_{p1} (mV)[b]
Re-nap	−1.53	−1.46	−1.92	−1.27	87
Re-ant	−1.24	−1.08	−1.52	−1.26	68
Re-pyr	−1.26	−1.26	−1.51	−1.44	91

[a] Measured in DMF at a scan rate of 0.1 Vs^{-1} [VAg/AgCl(sat)].
[b] ΔE_p was calculated for the second cathodic process from Fig. 6 (red line).

When cyclic voltammograms of the rhenium complexes were recorded (**Re-nap**, **Re-ant**, and **Re-pyr**), reduction peaks were observed between −1.2 and − 1.9 V, labeled E_1 and E_2, as shown in Fig. 6. The peaks observed in the reverse scan were labeled E_{1r} and E_{2r}. E_{1r} was related to the E_1 process, whereas E_{2r} was associated with the second, more cathodic wave E_2. In all cases, the E_1 reduction process (from −1.257 to −1.528 V) exhibited a quasi-reversible response. Conversely, E_2 was demonstrated to be a fully irreversible process for **Re-nap** (−1.923 V) and exhibited quasi-reversible behavior for **Re-ant** and **Re-pyr** at −1.518 and − 1.514 V, respectively. These patterns of quasi-reversible processes have also been observed in ruthenium complexes with aromatic substituents, such as anthracene- and pyrene-imidazo-phenanthroline moieties. In those systems, the first two redox processes were found to be reversible, consistent with the E_1 and E_2 peaks observed for the complexes investigated in the present work [74].

The more negative reduction potential observed for **Re-nap** indicates less effective stabilization of the reduced state than for **Re-ant** and **Re-pyr**. This trend can be attributed to the smaller π-conjugated system in the naphthalene fragment of **Re-nap**, which leads to a higher LUMO energy [91]. As a consequence, the molecule's ability to stabilize the added electron during reduction is diminished.

For all complexes, the E_1 process was attributed to the ligand-centered process resulting in the formation of an anion radical species, $[Re^{I}(L^{\bullet-})(CO)_3Cl]^-$ [99–102]. This species can experience slow chloride loss during the first reduction or rapid chloride dissociation during the second reduction. When the mechanism undergoes slow chlorine release, a characteristic reversible wave can be observed in the reverse scan (E_{1r}). The second quasi-reversible process (E_2) was assigned to a mostly metal-centered reduction (Re^{I} to Re^{0}), yielding a pentacoordinate species $[Re^{0}(L^{\bullet-})(CO)_3Cl]^-$ followed by a rapid Cl^- loss to form the formation of five-coordinate intermediate $[Re^{0}(L^{\bullet-})(CO)_3]^-$, which is capable of activating CO_2 [99–102]. These assignments were confirmed by observing the second oxidation wave (labeled E_{2r}) during the reverse scan, which can be attributed to the oxidation of the pentacoordinate species.

Scan-rate dependent cyclic voltammetry revealed that both ligands and complexes behave as molecular electroactive species in solution (Figs. S31 and S32). The cathodic currents increased with scan rate, showing an approximate $i_p \propto \nu^{1/2}$ dependence, consistent with a diffusion-controlled contribution to the redox response.

3.5. Electrocatalytic reduction of CO_2

In this study, we evaluated the electrocatalytic properties of three ligands (**nap**, **ant**, and **pyr**; Fig. S34) and their corresponding rhenium tricarbonyl complexes (**Re-nap**, **Re-ant**, and ***Re*-pyr**; Fig. S35). We performed CV measurements in DMF under both nitrogen (N_2) and carbon dioxide (CO_2) atmospheres to assess their CO_2-reduction responses.

Upon CO_2 saturation, all ligands showed increased cathodic currents, indicating apparent CO_2 reduction activity (Fig. 7). The non-catalytic peak current (i_p) was extracted from the cathodic scan recorded under N_2, using the cathodic peak associated with the main reduction event of each free ligand and the first cathodic wave for the Re complexes. In each case, i_p was obtained after local baseline correction. The catalytic current (i_{cat}) was determined from the CO_2-saturated voltammogram by subtracting the corresponding N_2 trace at the same potential (E_{cat}). E_{cat}, was selected as the potential that gave the maximum CO_2-enhanced cathodic response within the catalytic region [57,103]. Because the voltammograms do not exhibit ideal S-shaped catalytic waves, the extracted i_{cat}/i_p values should be interpreted as apparent comparative parameters rather than intrinsic kinetic constants. The i_{cat}/i_p ratio determined for the ligands and complexes is shown in Table 6.

Based on the i_{cat}/i_p ratio, the apparent catalytic response follows the order pyr = nap > ant, showing that the naphthalene and pyrene derivatives displayed comparable CO_2-induced cathodic current enhancement, while the anthracene analog is less active.

For the Re complexes, an enhancement in cathodic current upon CO_2 saturation was observed (Fig. 7), consistent with electrocatalytic CO_2 reduction. According to the i_{cat}/i_p ratio (Table 6), they exhibited greater cathodic current under a CO_2 atmosphere than free ligands, with **Re-pyr** showing the highest value, followed by **Re-nap** and **Re-ant**, which displayed comparable values. Although the reduction potential before the enhanced-cathodic current of the three Re complexes is nearly identical (~1.5 V), the catalytic current under CO_2 is almost twice as high for **Re-pyr** (9.13 μA) as for **Re-nap** (5.95 μA) and **Re-ant** (6.51 μA). This behavior suggests that the **pyr** ligand coordinated to the Re does not shift the thermodynamic potential for reduction. Instead, it appears to influence a later stage of the catalytic sequence, possibly by stabilizing reduced intermediates, enhancing electronic delocalization, or facilitating charge accumulation prior to the chemical step. Previous studies have shown that pyrene fragments can act not only as anchoring groups for graphitic electrodes, but also as electronic components that facilitate charge accumulation, catalyst-electrode communication, and even internal electron transfer [72,104–106].

Under CO_2, the cathodic currents also increased with scan rate for the ligands and Re complexes. The catalytic waves remained peak-shaped and scan-rate-dependent rather than reaching an ideal scan-rate-independent plateau. Although the scan-rate experiments confirm a reproducible enhancement of the cathodic current under CO_2, particularly for **Re-pyr**, they also indicate that the systems do not operate under an ideal kinetic plateau regime.

The use of i_{cat}/i_p as an apparent current-enhancement parameter is well established in Re-based molecular CO_2-reduction electrocatalysis. For example, Saha et al. illustrated the determination of i_{cat} and i_p for Re (I)-tpy carbonyl complexes from cyclic voltammetry measurements recorded under N_2 and CO_2, finding values of i_{cat}/i_p in the range of 7.1–9.6 at 0.1 Vs^{-1} in ACN [57]. Similarly, Talukdar et al. use the same

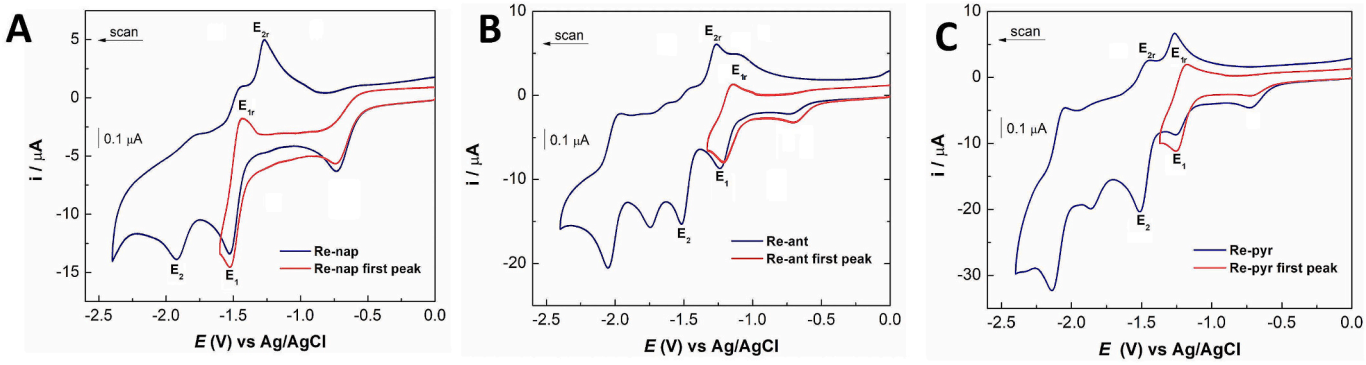


Fig. 6. Cyclic voltammograms in the cathodic branch for **Re-nap** (**A**), **Re-ant** (**B**), and **Re-pyr** (**C**) complexes. All measurements were recorded at a scan rate of 0.1 Vs^{-1} in DMF under nitrogen, with a 0.1 M $TBAPF_6$ supporting electrolyte.

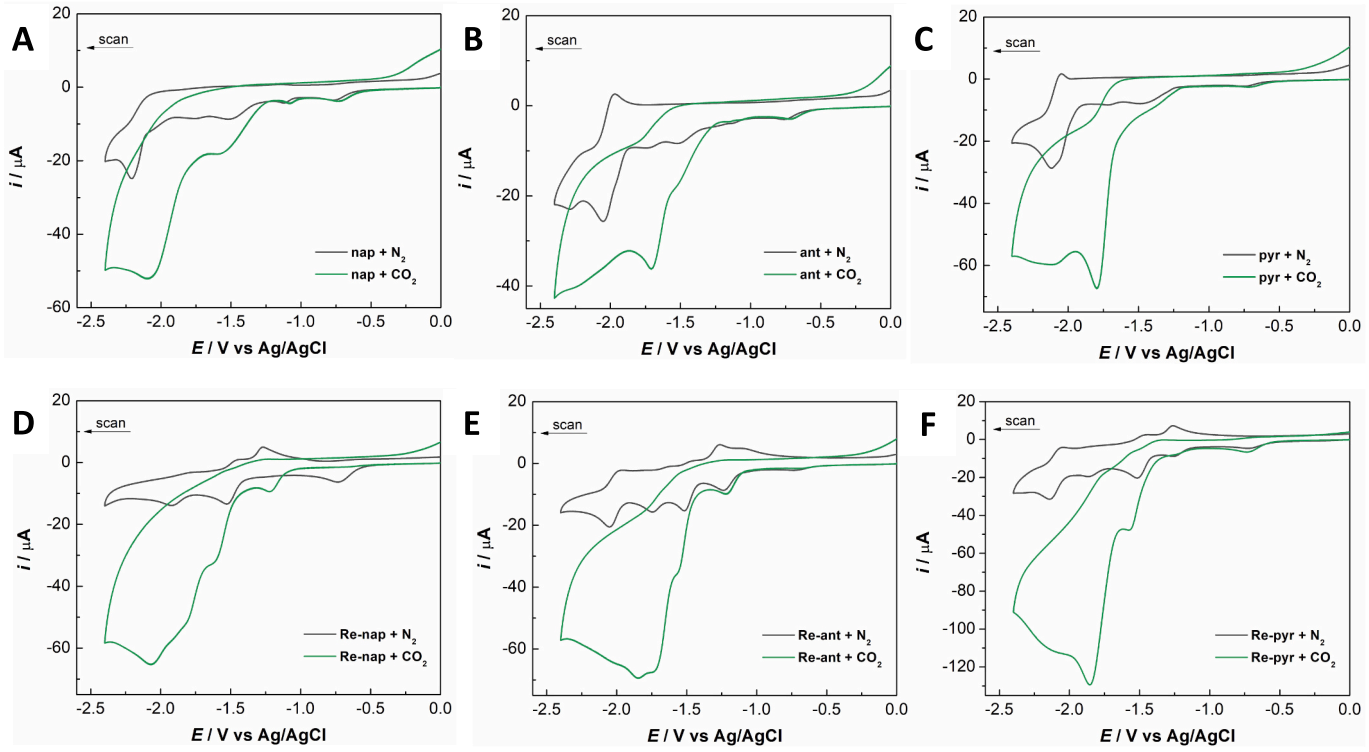


Fig. 7. Electrocatalytic effect for CO_2 reduction studied by cyclic voltammetry at 0.1 Vs^{-1} as a scan rate for (**A-C**) the free ligands and (**D—F**) rhenium(I) complexes.

Table 6
Summary of electrochemical CO_2 reduction for ligands and Re(I) complexes.

Compound	E_{pc} (V)	i_p (μA)	E_{cat} (V)	i_{cat} (μA)	i_{cat} / i_p[a]
Nap	−2.21	8.80	−2.09	40.0	4.54
Ant	−2.05	10.1	−1.71	27.0	2.69
Pyr	−2.11	12.8	−1.80	59.3	4.65
Re-nap	−1.52	5.95	−2.07	53.2	8.94
Re-ant	−1.51	6.51	−1.85	57.3	8.80
Re-pyr	−1.51	9.13	−1.85	110	12.0

[a] Values obtained by CV at 0.1 Vs^{-1}.

ratio to compare second-sphere hydrogen-bonding Re(I)-bpy catalysts, reporting values from 4.4 to 11 at 0.1 Vs^{-1} in ACN [55]. [Re(R_2phen)$(CO)_3$Cl] complexes, with (R_2phen = 2,9-disubstituted-1,10-phenanthroline) were also analyzed through i_{cat}/i_p with values from 4.1 - 14.8 at 0.2 Vs^{-1} in DMF, highlighting the influence of the electronic and steric properties of the ligand, and solvent on the observed activity [107]. In this context, the i_{cat}/i_p values obtained for **Re-nap**, **Re-ant**, and **Re-pyr** in the present study, featuring increased aromaticity in the fragment of the imidazo-phenanthroline ligand, fall within the range reported for active Re carbonyl CO_2-reduction catalysts. In addition, positioning **Re-pyr** approaching the higher-activity Re-phenanthroline systems.

These results demonstrate the potential of our complexes as versatile scaffolds, capable of consistent activity in two distinct areas: CO_2 electroreduction and singlet oxygen photosensitization.

4. Conclusions

In this work, a series of [Re$(CO)_3$(N—N)Cl] complexes bearing imidazo[4,5-*f*][1,10]phenanthroline ligands with systematically extended aromatic fragments; naphthalene (**nap**), anthracene (**ant**), and pyrene (**pyr**); was synthesized and evaluated to establish how increasing ligand aromaticity modulates structural, photophysical, singlet oxygen photosensitizing, and CO_2-responsive electrochemical properties. The crystal structure of **Re-nap** revealed a distorted octahedral Re(I) center and an almost coplanar naphthyl-imidazo-phenanthroline framework, with a dihedral angle of 2.56(10)°, supported by π-stacking interactions, indicating efficient structural communication across the ligand scaffold. Photophysical studies showed that the aromatic fragment governs the balance between IL, ILCT, and MLCT excited states: **Re-nap** displayed the most emissive and longest-lived ^{3}MLCT excited state, with Φ_{PL} = 1.90% and τ = 9354 ns in CH_2Cl_2, whereas **Re-ant** showed a lower quantum yield of PL and shorter lifetimes, and **Re-pyr** exhibited very weak MLCT emission, suggesting that the excited state decay of **Re-ant** and **Re-pyr** evolves to the anthracene or pyrene located triplet excited states. These different emissive behaviors are consistent with the singlet-oxygen sensitization increased across the series, with Φ_Δ values of 0.708, 0.844, and 0.887 for **Re-nap**, **Re-ant**, and **Re-pyr**, respectively. These results demonstrate that aromatic extension, particularly pyrene incorporation, enhances energy-transfer efficiency toward molecular oxygen. Electrochemical studies further revealed that the Re complexes exhibit greater CO_2-induced cathodic current enhancement than the free ligands, with apparent i_{cat}/i_p ratios of 8.94, 8.80, and 12.0 for **Re-nap**, **Re-ant**, and **Re-pyr**, respectively. In summary, these findings demonstrate that systematic aromatic extension -incorporating naphthalene, anthracene, and pyrene- constitutes an effective molecular design strategy to tune the excited-state behavior and functional electrochemical response of Re(I) imidazo-phenanthroline complexes, identifying the pyrene-containing derivative as the most promising platform for combined singlet-oxygen photosensitization and apparent CO_2 reduction activity.

Declaration of competing interest

The authors declare that they have no known competing financial interests or personal relationships that could have appeared to influence the work reported in this paper.

Acknowledgments

P.M.T.S acknowledges financial support from ANID Fondecyt de Iniciación en Investigación 11250976.

Appendix A. Supplementary data

Supplementary data to this article can be found online at https://doi.org/10.1016/j.ica.2026.123402.

Data availability

I have shared the original CIF and Checkcif files of the structure of the compound reported here.

2541193 (Original data) (CCDC)

References

[1] R.-Y. Wang, W.-L. Jia, H. Aziz, G. Vamvounis, S. Wang, N.-X. Hu, Z.D. Popović, J. A. Coggan, 1-Methyl-2-(anthryl)-imidazo[4,5-f][1,10]-phenanthroline: a highly efficient Electron-transport compound and a bright blue-light emitter for electroluminescent devices, Adv. Funct. Mater. 15 (2005) 1483–1487.

[2] J.-F. Lee, Y.-C. Chen, J.-T. Lin, C.-C. Wu, C.-Y. Chen, C.-A. Dai, C.-Y. Chao, H.-L. Chen, W.-B. Liau, Blue light-emitting and electron-transporting materials based on dialkyl-functionlized anthracene imidazophenanthrolines, Tetrahedron 67 (2011) 1696–1702.

[3] J. Peng, J. Sun, P. Gong, P. Xue, Z. Zhang, G. Zhang, R. Lu, Luminescent nanofibers fabricated from Phenanthroimidazole derivatives by Organogelation: fluorescence response towards acid with high performance, Chem. Asian J. 10 (2015) 1717–1724.

[4] S. Xiao, T. Yi, Y. Zhou, Q. Zhao, F. Li, C. Huang, Multi-state molecular switches based on dithienylperfluorocyclopentene and imidazo[4,5-f][1,10] phenanthroline, Tetrahedron 62 (2006) 10072–10078.

[5] Y. Liu, H. Liu, Q. Bai, C. Du, A. Shang, D. Jiang, X. Tang, P. Lu, Pyrene[4,5-d] imidazole-based derivatives with hybridized local and charge-transfer state for highly efficient blue and White organic light-emitting diodes with low efficiency roll-off, ACS Appl. Mater. Interfaces 12 (2020) 16715–16725.

[6] G. Umasankar, H. Ulla, C. Madhu, G.R. Reddy, B. Shanigaram, J.B. Nanubolu, B. Kotamarthi, G.V. Karunakar, M.N. Satyanarayan, V.J. Rao, Imidazole-pyrene hybrid luminescent materials for organic light-emitting diodes: synthesis, Characterization & Electroluminescent Properties, J. Mol. Struct. 1236 (2021) 130306.

[7] L. Li, J.-Q. Cao, H.-M. Liu, Q. Wu, Q.-H. Pan, Z.-P. Zeng, Y.-T. Lan, Y.-M. Li, W.-J. Mei, X.-C. Wang, W.-J. Zheng, Microwave-assisted synthesis of Imidazo[4,5-f] [1,10]phenanthroline derivatives as apoptosis inducers in chemotherapy by stabilizing Bcl-2 G-quadruplex DNA, Molecules 22 (2017) 829.

[8] S. Hu, W. Ma, J. Wang, Z. Zhou, Y. Ma, R. Zhang, K. Du, H. Zhang, M. Sun, X. Jiang, H. Tu, X. Tang, X. Yao, P. Chen, Synthesis and biological activity of 1H-imidazo[4,5-f][1,10]phenanthroline as a potential antitumor agent with PI3K/AKT/mTOR signaling, Eur. J. Pharmacol. 915 (2022) 174514.

[9] L.E. Kapp, M. Schutte-Smith, L. Twigge, H.G. Visser, Synthesis, characterization and DNA binding of four imidazo[4,5-f]1,10-phenanthroline derivatives, J. Mol. Struct. 1247 (2022) 131235.

[10] J. Walshe, P.M. Carron, S. McCormack, J. Doran, G. Amarandei, Organic luminescent down-shifting liquid beam splitters for hybrid photovoltaic-thermal (PVT) applications, Sol. Energy Mater. Sol. Cells 219 (2021) 110818.

[11] J. Walshe, P.M. Carron, C. McLoughlin, S. McCormack, J. Doran, G. Amarandei, Nanofluid development using silver nanoparticles and organic-luminescent molecules for solar-thermal and hybrid photovoltaic-thermal applications, Nanomaterials 10 (2020) 1201.

[12] K. Coldrick, J. Walshe, J. Doran, G. Amarandei, Evaluation of the photon contributions to the solar energy conversion for organic luminescent down-shifting liquid beam splitters in hybrid photovoltaic-thermal (PVT) applications using raytracing Monte Carlo simulations, Sol. Energy Mater. Sol. Cells 254 (2023) 112201.

[13] F. Pina, M.A. Bernardo, E. García-España, Fluorescent Chemosensors containing polyamine receptors, Eur. J. Inorg. Chem. 2000 (2000) 2143–2157.

[14] M.-A. Schmid, J. Brückmann, J. Bösking, D. Nauroozi, M. Karnahl, S. Rau, S. Tschierlei, Merging of a Perylene moiety enables a RuII photosensitizer with long-lived excited states and the efficient production of singlet oxygen, Chem. Eur. J. 28 (2022) e202103609.

[15] S. Naithani, T. Goswami, F. Thetiot, S. Kumar, Imidazo[4,5-f][1,10] phenanthroline based luminescent probes for anion recognition: recent achievements and challenges, Coord. Chem. Rev. 475 (2023) 214894.

[16] L. Sanhueza, S. Luco, F. Salas, I. González, S. Robles, M. Natali, A. Khodr, O. Margeat, C.M. Ruiz, D. Cortés-Arriagada, P. Dreyse, Iridium complexes based on 1H-imidazo[4,5-f][1,10]phenanthroline ligand: photophysical properties and light-emitting electrochemical cells characterization, Chem. Eur. J. 32 (2025) e02588.

[17] J. Liu, H. Shi, X. Huang, Q. Shen, G. Zhao, Efficient Photoelectrochemical reduction of CO_2 on Pyridyl covalent bonded ruthenium(II) based-photosensitizer, Electrochim. Acta 216 (2016) 228–238.

[18] M. Lämmle, B. Bagemihl, D. Nauroozi, L. Petermann, A. Pannwitz, S. Rau, Monosubstitution of 1H-Imidazo[4,5-f][1,10]phenanthroline ligands yields maximum luminescence quantum yield in ruthenium Polypyridyl complexes, ChemPhotoChem 6 (2022) e202200053.

[19] K. Choroba, M. Penkala, J. Palion-Gazda, E. Malicka, B. Machura, Pyrenyl-substituted Imidazo[4,5-f][1,10]phenanthroline rhenium(I) complexes with record-high triplet excited-state lifetimes at room temperature: steric control of Photoinduced processes in Bichromophoric systems, Inorg. Chem. 62 (2023) 19256–19269.

[20] S. Kumar, S. Singh, A. Kumar, K.S.R. Murthy, A. Kumar Singh, pH-responsive luminescence sensing, photoredox catalysis and photodynamic applications of ruthenium(II) photosensitizers bearing imidazo[4,5-f][1,10]phenanthroline scaffolds, Coord. Chem. Rev. 452 (2022) 214272.

[21] G.B. Bodedla, X. Zhu, Z. Zhou, W.-Y. Wong, Small molecules containing amphoteric imidazole motifs as sensitizers for dye-sensitized solar cells: an overview, Top. Curr. Chem. 380 (2022) 49.

[22] H.-L. Zhang, Y.-T. Yu, Y. Wang, Q. Tang, S.-P. Yang, J.-G. Liu, Visible light-controlled carbon monoxide delivery combined with the inhibitory activity of histone deacetylases from a manganese complex for an enhanced antitumor therapy, J. Inorg. Biochem. 216 (2021) 111354.

[23] G. Ghosh, H. Yin, S.M.A. Monro, T. Sainuddin, L. Lapoot, A. Greer, S. A. McFarland, Synthesis and characterization of Ru(II) complexes with π-expansive Imidazophen ligands for the Photokilling of human melanoma cells, Photochem. Photobiol. 96 (2020) 349–357.

[24] J. Kou, J. Shen, M. Lin, K. Xiong, L. Wang, F. Wei, J. Zhang, Synthesis and evaluation of four novel nitrogen-heterocyclic ruthenium polypyridyl complexes as photosensitizers for one and two-photon photodynamic therapy, Dalton Trans. 52 (2023) 6978–6986.

[25] S.B. Chanu, M.K. Raza, D. Musib, M. Pal, M. Pal, M. Roy, Potent photochemotherapeutic activity of Iron(III) complexes on visible light-induced ligand to metal charge transfer, Chem. Lett. 49 (2020) 724–727.

[26] B. Kar, P. Paira, Photostimulated anticancer activity of mitochondria localized rhenium(I) Tricarbonyl complexes bearing 1H-imidazo[4,5-f][1,10]phenanthroline ligands against MDA-MB-231 Cancer cells, Chem. Eur. J. 31 (2025) e202401720.

[27] D. Musib, M.K. Raza, S. Kundu, M. Roy, Modulating in vitro photodynamic activities of copper(II) complexes, Eur. J. Inorg. Chem. 2018 (2018) 2011–2018.

[28] S. Hostachy, C. Policar, N. Delsuc, Re(I) carbonyl complexes: multimodal platforms for inorganic chemical biology, Coord. Chem. Rev. 351 (2017) 172–188.

[29] A. Kumar, S.-S. Sun, A.J. Lees, Photophysics and photochemistry of organometallic rhenium Diimine complexes, in: A.J. Lees (Ed.), Photophysics of Organometallics, Springer-Verlag Berlin Heidelberg, 2010, pp. 37–71.

[30] A. Vlcek, Ultrafast excited-state processes in re(I) carbonyl-Diimine complexes: From excitation to photochemistry, in: A.J. Lees (Ed.), Photophysics of Organometallics, Springer-Verlag Berlin Heidelberg, 2010, pp. 115–158.

[31] Q. Qi, Q. Wang, Y. Li, D.Z. Silva, M.E. Ruiz, R. Ouyang, B. Liu, Y. Miao, Recent development of rhenium-based materials in the application of diagnosis and tumor therapy, Molecules 28 (2023) 2733.

[32] K.K.-W. Lo, K.Y. Zhang, S.P.-Y. Li, Recent exploitation of luminescent rhenium(I) Tricarbonyl Polypyridine complexes as biomolecular and cellular probes, Eur. J. Inorg. Chem. 2011 (2011) 3551–3568.

[33] H.C. Bertrand, S. Clède, R. Guillot, F. Lambert, C. Policar, Luminescence modulations of rhenium Tricarbonyl complexes induced by structural variations, Inorg. Chem. 53 (2014) 6204–6223.

[34] A.J. Amoroso, M.P. Coogan, J.E. Dunne, V. Fernández-Moreira, J.B. Hess, A. J. Hayes, D. Lloyd, C. Millet, S.J.A. Pope, C. Williams, Rhenium fac tricarbonyl bisimine complexes: biologically useful fluorochromes for cell imaging applications, Chem. Commun. (2007) 3066–3068.

[35] V. Fernández-Moreira, F.L. Thorp-Greenwood, A.J. Amoroso, J. Cable, J.B. Court, V. Gray, A.J. Hayes, R.L. Jenkins, B.M. Kariuki, D. Lloyd, C.O. Millet, C. F. Williams, M.P. Coogan, Uptake and localisation of rhenium fac-tricarbonyl polypyridyls in fluorescent cell imaging experiments, Org. Biomol. Chem. 8 (2010) 3888–3901.

[36] A. Leonidova, G. Gasser, Underestimated potential of organometallic rhenium complexes as anticancer agents, ACS Chem. Biol. 9 (2014) 2180–2193.

[37] R.M. Spada, M. Cepeda-Plaza, M.L. Gómez, G. Günther, P. Jaque, N. Pizarro, R. E. Palacios, A. Vega, Clean singlet oxygen production by a ReI complex embedded in a flexible self-standing polymeric Silsesquioxane film, J. Phys. Chem. C 119 (2015) 10148–10159.

[38] A. Kastl, S. Dieckmann, K. Wähler, T. Völker, L. Kastl, A.L. Merkel, A. Vultur, B. Shannan, K. Harms, M. Ocker, W.J. Parak, M. Herlyn, E. Meggers, Rhenium complexes with visible-light-induced anticancer activity, ChemMedChem 8 (2013) 924–927.

[39] I. Maisuls, T.M. Kirse, A. Hepp, J. Kösters, E. Wolcan, C.A. Strassert, Rhenium(I) complexes with neutral Monodentate Coligands and Monoanionic 2-(1,2,4-Triazol-5-yl)pyridine-based chelators as bidentate Luminophores with tunable color and photosensitized generation of $^1O_2$: an integrated Case study involving Photophysics and theory, Inorg. Chem. 61 (2022) 13775–13791.

[40] T.C. Pham, V.-N. Nguyen, Y. Choi, S. Lee, J. Yoon, Recent strategies to develop innovative photosensitizers for enhanced photodynamic therapy, Chem. Rev. 121 (2021) 13454–13619.

[41] R. Fernández-Terán, L. Sévery, Living long and prosperous: productive Intraligand charge-transfer states from a rhenium(I) Terpyridine photosensitizer with enhanced light absorption, Inorg. Chem. 60 (2021) 1334–1343.
[42] E. Wolcan, Photosensitized generation of singlet oxygen from rhenium(I) complexes: a review, Inorg. Chim. Acta 509 (2020) 119650.
[43] R. Kushwaha, V. Singh, S. Peters, A.K. Yadav, T. Sadhukhan, B. Koch, S. Banerjee, Comparative study of Sonodynamic and Photoactivated Cancer therapies with re (I)-Tricarbonyl complexes comprising Phenanthroline ligands, J. Med. Chem. 67 (2024) 6537–6548.
[44] S.-F. He, J.-X. Liao, M.-Y. Huang, Y.-Q. Zhang, Y.-M. Zou, C.-L. Wu, W.-Y. Lin, J.-X. Chen, J. Sun, Rhenium–guanidine complex as photosensitizer: trigger HeLa cell apoptosis through death receptor-mediated, mitochondria-mediated, and cell cycle arrest pathways, Metallomics 14 (2022) mfac008.
[45] R. Kushwaha, A. Upadhyay, S. Peters, A.K. Yadav, A. Mishra, A. Bera, T. Sadhukhan, S. Banerjee, Visible and red light-triggered anticancer profile of a ferrocene-re(I)-Tricarbonyl conjugate: experimental and theoretical studies, Langmuir 40 (2024) 12226–12238.
[46] M. Małecka, A. Szlapa-Kula, A.M. Maroń, P. Ledwon, M. Siwy, E. Schab-Balcerzak, K. Sulowska, S. Maćkowski, K. Erfurt, B. Machura, Impact of the Anthryl linking mode on the Photophysics and excited-state dynamics of re(I) complexes [ReCl(CO)3(4′-an-terpy-κ2N)], Inorg. Chem. 61 (2022) 15070–15084.
[47] N. Manav, P.E. Kesavan, M. Ishida, S. Mori, Y. Yasutake, S. Fukatsu, H. Furuta, I. Gupta, Phosphorescent rhenium-dipyrrinates: efficient photosensitizers for singlet oxygen generation, Dalton Trans. 48 (2019) 2467–2478.
[48] F. Ragone, H.H. Martinez Saavedra, P.M.D. Gara, G.T. Ruiz, E. Wolcan, Photosensitized generation of singlet oxygen from re(I) complexes: a Photophysical study using LIOAS and luminescence techniques, J. Phys. Chem. A 117 (2013) 4428–4435.
[49] S. Monro, K.L. Colón, H. Yin, J. Roque, P. Konda, S. Gujar, R.P. Thummel, L. Lilge, C.G. Cameron, S.A. McFarland, Transition metal complexes and photodynamic therapy from a tumor-centered approach: challenges, opportunities, and highlights from the development of TLD1433, Chem. Rev. 119 (2019) 797–828.
[50] K.K.-W. Lo, Exploitation of luminescent organometallic rhenium(I) and iridium (III) complexes in biological studies, in: A.J. Lees (Ed.), Photophysics of Organometallics, Springer-Verlag Berlin Heidelberg, 2010, pp. 73–114.
[51] K.A. Wells, J.E. Yarnell, J.R. Palmer, T.S. Lee, C.M. Papa, F.N. Castellano, Energy migration processes in re(I) MLCT complexes featuring a Chromophoric ancillary ligand, Inorg. Chem. 59 (2020) 8259–8271.
[52] J.E. Yarnell, K.A. Wells, J.R. Palmer, J.M. Breaux, F.N. Castellano, Excited-state triplet equilibria in a series of re(I)-Naphthalimide Bichromophores, J. Phys. Chem. B 123 (2019) 7611–7627.
[53] J.E. Yarnell, J.C. Deaton, C.E. McCusker, F.N. Castellano, Bidirectional "ping-pong" energy transfer and 3000-fold lifetime enhancement in a re(I) charge transfer complex, Inorg. Chem. 50 (2011) 7820–7830.
[54] X. Yi, J. Zhao, W. Wu, D. Huang, S. Ji, J. Sun, Rhenium(i) tricarbonyl polypyridine complexes showing strong absorption of visible light and long-lived triplet excited states as a triplet photosensitizer for triplet–triplet annihilation upconversion, Dalton Trans. 41 (2012) 8931–8940.
[55] K. Talukdar, S. Sinha Roy, E. Amatya, E.A. Sleeper, P. Le Magueres, J.W. Jurss, Enhanced electrochemical CO_2 reduction by a series of molecular rhenium catalysts decorated with second-sphere hydrogen-bond donors, Inorg. Chem. 59 (2020) 6087–6099.
[56] K.A. Grice, C.P. Kubiak, Chapter five - recent studies of rhenium and manganese Bipyridine carbonyl catalysts for the electrochemical reduction of CO_2, Adv. Inorg. Chem. 66 (2014) 163–188.
[57] S. Saha, T. Doughty, D. Banerjee, S.K. Patel, D. Mallick, E.S. Subramaniam Iyer, S. Roy, R. Mitra, Electrocatalytic reduction of CO_2 to CO by a series of organometallic re(i)-tpy complexes, Dalton Trans. 52 (2023) 15394–15411.
[58] J. Hawecker, J.-M. Lehn, R. Ziessel, Electrocatalytic reduction of carbon dioxide mediated by Re(bipy)$(CO)_3$Cl (bipy = 2,2′-bipyridine), J. Chem. Soc. Chem. Commun. (1984) 328–330.
[59] Y. Liang, M.T. Nguyen, B.J. Holliday, R.A. Jones, Electrocatalytic reduction of CO2 using rhenium complexes with dipyrido[3,2-a:2′,3′-c]phenazine ligands, Inorg. Chem. Commun. 84 (2017) 113–117.
[60] J.K. Nganga, C.R. Samanamu, J.M. Tanski, C. Pacheco, C. Saucedo, V.S. Batista, K. A. Grice, M.Z. Ertem, A.M. Angeles-Boza, Electrochemical reduction of CO_2 catalyzed by re(pyridine-oxazoline)$(CO)_3$Cl complexes, Inorg. Chem. 56 (2017) 3214–3226.
[61] P.M. Toro, M. Henríquez, I. Erazo, P. Levín, D. Villaman, M. Natali, C. Barrientos, A.R. Cabrera, Rhenium (I) complexes based on iminopyridyl ligands: structural, photophysical, and CO_2 electrocatalytic reduction studies, Inorg. Chim. Acta 587 (2025) 122827.
[62] L. Rotundo, S. Ahmad, C. Cappuccino, D.E. Polyansky, M.Z. Ertem, G.F. Manbeck, A Dicationic fac-re(bpy)$(CO)_3$Cl for CO_2 Electroreduction at a reduced Overpotential, Inorg. Chem. 62 (2023) 7877–7889.
[63] A.N. Hellman, J.A. Intrator, J.C. Choate, D.A. Velazquez, S.C. Marinescu, Primary- and secondary-sphere effects of amine substituent position on rhenium bipyridine electrocatalysts for CO_2 reduction, Polyhedron 223 (2022) 115933.
[64] J.D.B. Koenig, Z.S. Dubrawski, K.R. Rao, J. Willkomm, B.S. Gelfand, C. Risko, W. E. Piers, G.C. Welch, Lowering Electrocatalytic CO_2 reduction Overpotential using N-annulated Perylene Diimide rhenium Bipyridine dyads with variable tether length, J. Am. Chem. Soc. 143 (2021) 16849–16864.
[65] L. Rotundo, C. Garino, E. Priola, D. Sassone, H. Rao, B. Ma, M. Robert, J. Fiedler, R. Gobetto, C. Nervi, Electrochemical and photochemical reduction of CO2 catalyzed by re(I) complexes carrying local proton sources, Organometallics 38 (2019) 1351–1360.
[66] M.L. Clark, P.L. Cheung, M. Lessio, E.A. Carter, C.P. Kubiak, Kinetic and mechanistic effects of Bipyridine (bpy) substituent, labile ligand, and Brønsted acid on Electrocatalytic CO_2 reduction by re(bpy) complexes, ACS Catal. 8 (2018) 2021–2029.
[67] W. Yang, S. Sinha Roy, W.C. Pitts, R.L. Nelson, F.R. Fronczek, J.W. Jurss, Electrocatalytic CO_2 reduction with Cis and trans conformers of a rigid Dinuclear rhenium complex: comparing the monometallic and cooperative bimetallic pathways, Inorg. Chem. 57 (2018) 9564–9575.
[68] C.W. Machan, J. Yin, S.A. Chabolla, M.K. Gilson, C.P. Kubiak, Improving the efficiency and activity of Electrocatalysts for the reduction of CO_2 through supramolecular assembly with amino acid-modified ligands, J. Am. Chem. Soc. 138 (2016) 8184–8193.
[69] S.A. Roell, B.R. Schrage, C.J. Ziegler, T.A. White, Isolating substituent effects in re (I)-phenanthroline electrocatalysts for CO_2 reduction, Inorg. Chim. Acta 503 (2020) 119397.
[70] A.M. Abudayyeh, S. De Kreijger, S. Grau, E. Eryılmaz, K. Robeyns, M.Z. Ertem, A. Llobet, B. Elias, L. Troian-Gautier, Enhanced Electrocatalytic and selective CO_2-to-CO reduction by a rhenium(I) complex bearing 6,6′-substituted 2,2′-Bipyridines, ACS Catal. 16 (2026) 542–554.
[71] S. Pizarro, J. Becerra, C. Angel, R. Cañas-Sarazua, A. Delgadillo, CO_2 capture: exploring rhenium complexes as redox mediators, Inorg. Chem. 64 (2025) 10637–10644.
[72] S. Sinha, A. Sonea, W. Shen, S.S. Hanson, J.J. Warren, Heterogeneous aqueous CO_2 reduction using a pyrene-modified rhenium(I) Diimine complex, Inorg. Chem. 58 (2019) 10454–10461.
[73] S.A. Chabolla, E.A. Dellamary, C.W. Machan, F.A. Tezcan, C.P. Kubiak, Combined steric and electronic effects of positional substitution on dimethyl-bipyridine rhenium(I)tricarbonyl electrocatalysts for the reduction of CO_2, Inorg. Chim. Acta 422 (2014) 109–113.
[74] M. Mariappan, B.G. Maiya, Effects of anthracene and pyrene units on the interactions of novel polypyridylruthenium(II) mixed-ligand complexes with DNA, Eur. J. Inorg. Chem. (2005) 2164–2173.
[75] S.S. Bhat, A.A. Kumbhar, H. Heptullah, A.A. Khan, V.V. Gobre, S.P. Gejji, V. G. Puranik, Synthesis, electronic structure, DNA and protein binding, DNA cleavage, and anticancer activity of fluorophore-labeled copper(II) complexes, Inorg. Chem. 50 (2011) 545–558.
[76] Bruker, APEX4, Bruker AXS Inc., Madison, Wisconsin, USA, 2021.
[77] G.M. Sheldrick, SADABS, Program for Empirical Absorption Correction of Area Detector Data, 1996.
[78] G.M. Sheldrick, SHELXT - integrated space-group and crystal-structure determination, Acta Crystallogr. A 71 (2015) 3–8.
[79] G.M. Sheldrick, Crystal structure refinement with SHELXL, Acta Crystallogr. C 71 (2015) 3–8.
[80] O.V. Dolomanov, L.J. Bourhis, R.J. Gildea, J.A.K. Howard, H. Puschmann, OLEX2: a complete structure solution, refinement and analysis program, J. Appl. Crystallogr. 42 (2009) 339–341.
[81] K. Suzuki, A. Kobayashi, S. Kaneko, K. Takehira, T. Yoshihara, H. Ishida, Y. Shiina, S. Oishi, S. Tobita, Reevaluation of absolute luminescence quantum yields of standard solutions using a spectrometer with an integrating sphere and a back-thinned CCD detector, Phys. Chem. Chem. Phys. 11 (2009) 9850–9860.
[82] F. Wilkinson, W.P. Helman, A.B. Ross, Quantum yields for the photosensitized formation of the lowest electronically excited singlet state of molecular oxygen in solution, J. Phys. Chem. Ref. Data Monogr. 22 (1993) 113–262.
[83] R. Schmidt, C. Tanielian, R. Dunsbach, C. Wolff, Phenalenone, a universal reference compound for the determination of quantum yields of singlet oxygen O2(1Δg) sensitization, J. Photochem. Photobiol. A Chem. 79 (1994) 11–17.
[84] L.E. Enslin, K. Purkait, M.D. Pozza, B. Saubamea, P. Mesdom, H.G. Visser, G. Gasser, M. Schutte-Smith, Rhenium(I) Tricarbonyl complexes of 1,10-Phenanthroline derivatives with unexpectedly high cytotoxicity, Inorg. Chem. 62 (2023) 12237–12251.
[85] D.R. Case, A. Spear, A.F. Henwood, M. Nanao, S. Dampf, T.M. Korter, T. Gunnlaugsson, J. Zubieta, R.P. Doyle, [re$(CO)_3$(5-PAN)cl], a rhenium(i) naphthalimide complex for the visible light photocatalytic reduction of CO_2, Dalton Trans. 50 (2021) 3479–3486.
[86] J.-X. Wang, H.-Y. Xia, W.-Q. Liu, F. Zhao, Y. Wang, Synthesis, spectroscopic, and DFT studies of rhenium(I) complexes with phenanthrolineimidazo ligands containing thienyl moieties, Inorg. Chim. Acta 394 (2013) 92–97.
[87] S.F. Haddad, J.A. Marshall, G.A. Crosby, B. Twamley, *Fac*-Tricarbonylchloro (1,10-phenanthroline)rhenium(I), Acta Crystallogr. E. 58 (2002) m559–m561.
[88] S.C. Marker, S.N. MacMillan, W.R. Zipfel, Z. Li, P.C. Ford, J.J. Wilson, Photoactivated in vitro anticancer activity of rhenium(I) Tricarbonyl complexes bearing water-soluble phosphines, Inorg. Chem. 57 (2018) 1311–1331.
[89] D. Magde, M.D. Magde, E.C. Glazer, So-called "dual emission" for ^{3}MLCT luminescence in ruthenium complex ions: what is really happening? Coord. Chem. Rev. 306 (2016) 447–467.
[90] G.J. Wilson, A. Launikonis, W.H.F. Sasse, A.W.-H. Mau, Excited-state processes in ruthenium(II) Bipyridine complexes containing covalently bound Arenes, J. Phys. Chem. A 101 (1997) 4860–4866.
[91] J. Wang, S. Xu, F. Zhao, H. Xia, Y. Wang, Computational and spectroscopic studies of the imidazole-fused phenanthroline derivatives containing phenyl, naphthyl, and anthryl groups, J. Mol. Struct. 1108 (2016) 46–53.
[92] J.A. Mondal, G. Ramakrishna, A.K. Singh, H.N. Ghosh, M. Mariappan, B.G. Maiya, T. Mukherjee, D.K. Palit, Ultrafast intramolecular electronic energy-transfer dynamics in a Bichromophoric molecule, J. Phys. Chem. A 108 (2004) 7843–7852.

[93] A. Szłapa-Kula, J. Palion-Gazda, P. Ledwon, K. Erfurt, B. Machura, A fundamental role of the solvent polarity and remote substitution of the 2-(4-R-phenyl)-1*H*-imidazo[4,5-*f*][1,10]phenanthroline framework in controlling the ground- and excited-state properties of re(I) chromophores [$ReCl(CO)_3$(R-C_6H_4-imphen)], Dalton Trans. 51 (2022) 14466–14481.
[94] S. Cui, X. Guo, S. Wang, Z. Wei, D. Huang, X. Zhang, T.C. Zhu, Z. Huang, Singlet oxygen in photodynamic therapy, Pharmaceuticals 17 (2024) 1274.
[95] J. Ferguson, T. Iredale, J.A. Taylor, The phosphorescene spectra of naphthalene and some simple derivatives, J. Chem. Soc. (1954) 3160–3165.
[96] M.R. Padhye, S.P. McGlynn, M. Kasha, Lowest triplet state of anthracene, J. Chem. Phys. 24 (1956) 588–594.
[97] D.F. Evans, 257. Perturbation of singlet–triplet transitions of aromatic molecules by oxygen under pressure, J. Chem. Soc. (1957) 1351–1357.
[98] Y. Yang, J. Brückmann, W. Frey, S. Rau, M. Karnahl, S. Tschierlei, Electron storage capability and singlet oxygen productivity of a RuII photosensitizer containing a fused Naphthaloylenebenzene moiety at the 1,10-Phenanthroline ligand, Chem. Eur. J. 26 (2020) 17027–17034.
[99] J. Mukherjee, I. Siewert, Manganese and rhenium Tricarbonyl complexes equipped with proton relays in the electrochemical CO_2 reduction reaction, Eur. J. Inorg. Chem. 2020 (2020) 4319–4333.
[100] Y. Hayashi, S. Kita, B.S. Brunschwig, E. Fujita, Involvement of a binuclear species with the Re−C(O)O−Re moiety in CO2 reduction catalyzed by tricarbonyl rhenium(I) complexes with diimine ligands: strikingly slow formation of the Re−Re and Re−C(O)O−Re species from Re(dmb)(CO)3S (dmb = 4,4‘-dimethyl-2,2,‘-bipyridine, S = solvent), J. Am. Chem. Soc. 125 (2003) 11976–11987.
[101] T. Morimoto, T. Nakajima, S. Sawa, R. Nakanishi, D. Imori, O. Ishitani, CO_2 capture by a rhenium(I) complex with the aid of Triethanolamine, J. Am. Chem. Soc. 135 (2013) 16825–16828.
[102] B.P. Sullivan, C.M. Bolinger, D. Conrad, W.J. Vining, T.J. Meyer, One- and two-electron pathways in the electrocatalytic reduction of CO_2 by fac-Re(bpy)$(CO)_3$Cl (bpy = 2,2′-bipyridine), J. Chem. Soc. Chem. Commun. (1985) 1414–1416.
[103] R. Francke, B. Schille, M. Roemelt, Homogeneously catalyzed Electroreduction of carbon dioxide—methods, mechanisms, and catalysts, Chem. Rev. 118 (2018) 4631–4701.
[104] J.D. Blakemore, A. Gupta, J.J. Warren, B.S. Brunschwig, H.B. Gray, Noncovalent immobilization of Electrocatalysts on carbon electrodes for fuel production, J. Am. Chem. Soc. 135 (2013) 18288–18291.
[105] B. Reuillard, K.H. Ly, T.E. Rosser, M.F. Kuehnel, I. Zebger, E. Reisner, Tuning product selectivity for aqueous CO_2 reduction with a Mn(bipyridine)-pyrene catalyst immobilized on a carbon nanotube electrode, J. Am. Chem. Soc. 139 (2017) 14425–14435.
[106] B.X. Nguyen, X. Li, J.J. Warren, Design and implementation of a CO_2 reduction catalyst with an internal Electron transfer mediator: improving turnover frequency by more than 10-fold, ACS Catal. 14 (2024) 12260–12268.
[107] B.J. Neyhouse, T.A. White, Modifying the steric and electronic character within re (I)-phenanthroline complexes for electrocatalytic CO_2 reduction, Inorg. Chim. Acta 479 (2018) 49–57.